Physics and Chemistry of the Earth 141 (2025) 104138

Contents lists available at ScienceDirect

Physics and Chemistry of the Earth

journal homepage: www.elsevier.com/locate/pce

Machine learning-based mapping of fog water harvesting potential in Pithoragarh, Uttarakhand: Evaluating climate scenarios and geospatial influences

Chiranjit Singha [a], Kishore Chandra Swain [a], Biswajeet Pradhan [b], Armin Moghimi [c], Babak Ranjgar [d,*], Shahid Gulzar [e], Hetvi Shah [e]

[a] Department of Agricultural Engineering, Institute of Agriculture, Visva-Bharati (A Central University), Sriniketan, Birbhum, West Bengal, 731236, India
[b] Centre for Advanced Modelling and Geospatial Information Systems (CAMGIS), School of Civil and Environmental Engineering, Faculty of Engineering and IT, University of Technology Sydney, Sydney, NSW, 2007, Australia
[c] Department of Photogrammetry and Remote Sensing, Geomatics Engineering Faculty, K. N. Toosi University of Technology, Tehran, 19967-15433, Iran
[d] Department of Energy, Politecnico di Milano, Milan, Italy
[e] Department of Geoinformatics, International Institute of Geospatial Science and Technology (IIGST), 87/210, Raja S.C. Mallick Road, Kolkata, 700047, India

ARTICLE INFO

Keywords:
Fog water harvesting
Machine learning model
Boruta algorithm
CMIP6
Sustainable development goal

ABSTRACT

Fog is crucial to the hydrological processes in Pithoragarh district, Uttarakhand, significantly affecting local water systems and ecosystems. This study employed five machine learning (ML) models, Gradient Boosting Machine (GBM), AdaBoost (ADB), Model Averaged Neural Network (avNNet), Naive Bayes (NB), and Shrinkage Discriminant Analysis (SDA) to map fog water potential in the area. Using data from 100 foggy locations and 23 variables (hydro-climatic, topographical, and terrain), the models were rigorously evaluated. Results showed that GBM, ADB, avNNet, NB, and SDA models identified high fog water potentiality classes in 43.91 %, 43.84 %, 44.79 %, 42.97 %, and 34.16 % of the area, respectively. ADB and GBM performed best (AUC = 0.999), followed by avNNet (AUC = 0.967), SDA (AUC = 0.967), and NB (AUC = 0.941). Key factors influencing fog occurrence included elevation, wind speed, wind exposition index, relative humidity, and mean power density, identified using the ordinary least square (OLS), various nature-inspired algorithms (such as GA, PSO, GO, DFO, HHO, and GWO), Pearson correlation, and Boruta sensitivity analysis. In this investigation, the linear regression approach was also applied to utilize ensembles of EC-Earth3, NorESM2-LM, and MIROC6 CMIP6 models for fog water forecasting climate conditions spanning from 2025 to 2055. Approximately 22.81 % and 21.52 % of the study area consistently exhibit very high potential for fog water harvesting (FWH) under the ssp245 and ssp585 scenarios, respectively. This research lays a foundation for addressing environmental concerns related to FWH and represents a significant step towards mitigating water scarcity, contributing to water security in the eastern Himalayas in line with Sustainable Development Goal 6 (SDG 6).

1. Introduction

Water is essential for human health and the well-being of ecosystems and societies (Cheng et al., 2021). Nonetheless, issues such as freshwater scarcity and pollution threaten its availability, leaving millions without access to safe water, a situation expected to worsen by 2025 (WHO, 2023). Climate change exacerbates this issue by increasing water demand, particularly in Southeast Asia and other developing regions, due to rising consumption (Ismail and Go, 2021). This situation necessitates the efficient use of resources and the exploration of new water sources (Feng et al., 2020).

Fog water harvesting (FWH) provides a sustainable and cost-effective solution by harnessing atmospheric humidity to supply fresh water, effectively addressing water scarcity in water-stressed regions (ASEAN, 2015; Al-Jawad et al., 2019; Khoury et al., 2023; Yu et al., 2021; Han and Guo, 2021; Elashmawy, 2020; Jarimi et al., 2020; Hoekstra et al., 2017; Fessehaye et al., 2017). This approach aligns with the UN Sustainable Development Goal 6 (SDG 6), which advocates for universal access to clean water and improved local availability (Shanyengana et al., 2003, Fessehaye et al., 2013). In regions like

* Corresponding author.
E-mail address: babak.ranjgar@polimi.it (B. Ranjgar).

https://doi.org/10.1016/j.pce.2025.104138
Received 14 November 2024; Received in revised form 29 July 2025; Accepted 6 October 2025
Available online 16 October 2025

Southern Bolivia, FWH is used for fog-based irrigation to secure food supplies (Castelli et al., 2023). In Southeast Asia, it helps reduce dependence on conventional water sources such as wells (Vanham, 2016; Zhou and Dai, 2017; Kutty et al., 2014). The successful application of this technology in countries including Canada, Saudi Arabia, and Chile further demonstrates its effectiveness (Gandhidasan et al., 2018; Olivier, 2002; LeBoeuf and de la Jara, 2014; Marzol and Sanchez, 2008; Fessehaye et al., 2015; Henderson and Falk, 2001; Ritter et al., 2015).

In such contexts, accurately identifying potential fog water sources is essential for conducting effective cost–benefit analyses, minimizing expenses, and ensuring project feasibility (Domen et al., 2013; Kutty et al., 2014). Geographic Information System (GIS) and Remote Sensing (RS) are invaluable tools for planning and selecting suitable sites for FWH systems. For example, Pretorius (2009) utilized GIS-RS methods in South Africa to locate potential FWH sites by evaluating factors such as elevation and slope, which provide safe drinking water to remote mountainous communities. Similarly, Fessehaye et al. (2015) used NASA's Aqua/Terra satellite imagery to assess fog feasibility in Eritrea, while Choudhury et al. (2007) applied NOAA-AVHRR data to map fog distribution in northern India. These studies demonstrate that by leveraging GIS/RS techniques and analyzing geospatial factors (e.g., wind speed, air temperature, and humidity), it is possible to identify optimal FWH locations, ensuring efficient resource use and reliable water supply for communities.

These international experiences demonstrate that FWH can be adapted for regions like Uttarakhand, where water scarcity is intensifying due to climate change and population growth, affecting many villages (NITI Aayog, 2019, Nand et al., 2017, Singh et al., 2015, Ground Water Year Book, Uttarakhand −2022, Singh, 2016). Identifying potential FWH sites in this region could benefit rural populations by providing fresh drinking water, supporting agriculture, enhancing livelihoods, and improving health and hygiene. While FWH might only meet a portion of the total water needs, it can significantly enhance the overall well-being of these communities.

While previous FWH studies have focused on modeling fog dynamics using hydrological variables, these approaches often require extensive datasets and complex computations (Qadir et al., 2018; Qadir et al., 2021; Gandhidasan et al., 2018; Mistry and Hurst, 2022). In recent years, research has shifted toward integrating Machine Learning (ML) algorithms with RS and GIS data for socio-environmental modeling in FWH. For instance, Karimidastenaei et al. (2019) introduced the Fog-water Harvesting Capability Index (FCI), which employs conditioning factors and ML models to identify ideal FWH sites. Despite its promise, this approach considered a limited number of factors and models.

To enhance FWH, our study investigates the use of advanced ML models to identify fog-prone areas in the Pithoragarh district under current and projected climate change conditions. Recognizing the significant impact of geo-environmental factors such as topography, hydrological conditions, and climate on fog formation (Haghighi et al., 2019; Karimidastenaei et al., 2019), we incorporate these variables as inputs for our modeling. We employ a set of ML models, including Gradient Boosting Machine (GBM), AdaBoost (ADB), Averaged Neural Network (avNNet), Naive Bayes (NB), and Shrinkage Discriminant Analysis (SDA), to produce detailed FWH distribution maps. Our framework leverages diverse environmental variables and RS imagery to create comprehensive maps that identify potential FWH sites. Additionally, we evaluate the future prospects of FWH by analyzing climate model simulations from EC-Earth3, NorESM2-LM, and MIROC6 under the CMIP6 framework's ssp245 and ssp585 scenarios for the period 2025-2055.

2. Material and methods

2.1. Study area

The study area lies in the southern part of the Central Himalayas, within the Pithoragarh district of Uttarakhand, India (80°–81°E, 29°4′–30°3′N), at an elevation of ~1,645 m above mean sea level (Fig. 2), covering an area of about 489.26 km^2. Pithoragarh has a temperate climate characterized by distinct seasonal variations in temperature. The region receives most of its rainfall (~166 mm annually) during the southwest monsoon and experiences around 140 rainy days per year. January is typically the coldest month (average temperature of 3.23 °C), while May is the hottest, with temperatures often exceeding 33 °C. During winter, members of the Bhotiya tribe migrate to lower altitudes with their livestock.

Pithoragarh hosts diverse water sources, including lakes, springs, and groundwater reserves. However, these resources have become increasingly threatened due to climate change, over-extraction, rapid urbanization, and population growth. Agriculture, the primary consumer of water in the state, accounts for a substantial proportion of total demand (URL: https://prepdata.org/dashboards/uttarakhand-water-resources).

Fig. 2 illustrates a declining trend in precipitation from 1960 to 2023 based on TerraClimate data. This observation aligns with the results of the Mann-Kendall trend test at rain gauge stations in Pithoragarh and Chamoli, both showing significant changes in precipitation ($p < 0.05$; Supplementary Table 1). In addition, GRACE satellite data (2002–2023) reveal a sharp decline in equivalent water thickness (EWT), decreasing from 42.099 cm to −121.367 cm, with annual losses ranging from −5.65 to −6.79 cm. These findings indicate increasing water stress in the region and highlight its potential for adopting FWH as a sustainable water management strategy, particularly under changing climate conditions.

2.2. Inventory of fog sampling

The upper regions of our study area are highly susceptible to winter valley fog, driven by cold air settling in low-lying terrain, and are influenced by local hydro-meteorological and orographic conditions (Sánchez-Falfan et al., 2023). To support spatial modeling of FWH, we conducted ground-based fog sampling at 200 georeferenced locations, including key locations such as Bassey, Sirtha, Hallpat, and Karma (see Fig. 1). These sampling points were selected based on historical meteorological data, fog frequency, temperature, humidity, visibility, and field reconnaissance.

Field campaigns were conducted during the peak fog periods in December and January of 2021 and 2022, with additional surveys in October and November 2022 to capture seasonal variations. Observations were recorded between 6:00 and 8:00 a.m., when fog conditions were most stable. Each site was geolocated using a Garmin eTrex 20 GPS, with on-site measurements of air temperature, humidity, and visibility collected using handheld sensors and visual assessments. Locations with recurring dense fog (visibility less than 500 m) were prioritized to enhance ground-truth data reliability. To ensure spatial representativeness, the sampling included various elevation bands, orientations, and proximities to land use features such as built-up areas, ridges, and valleys. Local knowledge was also used to identify microzones with historically persistent fog. The sampling data were converted into a binary format for model training and validation, with "1″ indicating the presence of fog and "0″ indicating its absence. The dataset was then divided using a 70:30 train-test split, where 140 plots were allocated for training the model and 60 plots were reserved for testing.

2.3. FWH factors

The present study utilized multiple RS data sources, including TRMM, NOAH FLDAS, SRTM DEM, ESA World Cover, Landsat 8, and

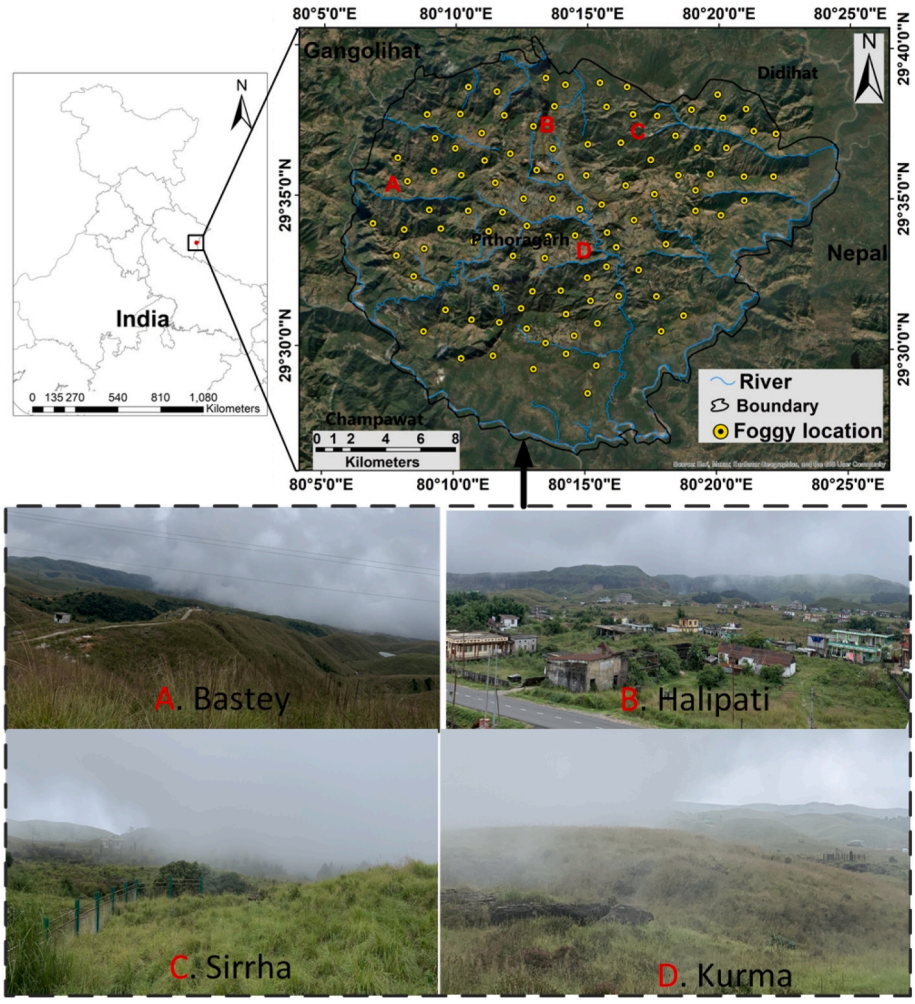

Fig. 1. Study area showing the Pithoragarh region with Field photographs of fog sampling ground location; (A) Bastey (29°58'04"N, 80°17'06"°E), (B) Halipati (29°06' 08" N, 80°22'04" E), (C) Sirrha (29°01'20" N, 80°30'08" E), and (D) Kurma (29°55' 07" N, 80°24'20"10° E).

Sentinel-2B, to assess the potential of fog water resources in the Pithoragarh region, Uttarakhand, India (Table 1). A total of twenty-three key topographic, environmental, and climatic parameters influencing fog formation were selected based on previous research (Karimidastenaei et al., 2019). These variables were categorized into three groups based on their relevance and interdependency: hydroclimatic parameters (precipitation (Pr), minimum and maximum (Tmax, Tmin) temperature, vapour pressure (VAP), wind exposition index (WEI), wind speed (WS), mean power density (PD), diurnal anisotropy heating (DAH) and topographic wetness index(TWI)), topographical parameters (elevation, aspect, slope, curvature, terrain ruggedness index (TRI), and topographic positional index(TPI)), and terrain distribution parameters (land use/land cover, land surface temperature (LST), distance to roads (DistRoad), distance to river (DistRiver), distance to buildings (DistBuildings), and normalized vegetation index (NDVI)). The Pr, Tmax, Tmin, RH, and WS parameters were used to project FWH trends using ensembles of EC-Earth3, NorESM2-LM, and MIROC6 CMIP6 models under the CMIP6 framework's SSP2-4.5 and SSP5-8.5 scenarios from 2025-2055.

In our processing workflow, all temporal features were averaged on an annual basis to ensure consistency. Along with other raster layers, they were then resampled to a spatial resolution of 30 × 30 m using bilinear interpolation, preparing them for the implementation of ML models. This process was carried out using R (version 4.4.0), Python (version 3.10), and ArcGIS (version 10.7). The computational tasks were performed on a desktop computer equipped with an Intel® Core™ i7-5700HQ CPU (3.50 GHz), 32 GB RAM, and an NVIDIA GeForce GTX 970M GPU, running Windows 10.

2.3.1. *Topographical parameters*

2.3.1.1. Elevation. Elevation enhances FWH by increasing exposure to fog-laden air, especially in mountainous regions where cooler temperatures and orographic lifting promote fog formation (Fessehaye et al., 2013). This study utilized elevation data from the U.S. Geological Survey (USGS) Digital Elevation Model (DEM) accessed via Google Earth Engine (GEE), using the "USGS/SRTMGL1_003″ dataset, which provides 30-m resolution layers (Fig. 3a). The study area's elevation ranges from 416 to 2474 m, with a mean of approximately 1426 m.

2.3.1.2. Slope. Topographic slope influences FWH by affecting fog interception and airflow dynamics. Moderate slopes enhance droplet capture efficiency, while steep slopes may hinder infrastructure stability and increase runoff loss (Schemenauer and Cereceda, 1994). A slope angle map was generated from DEM data using ArcGIS 10.7's "Spatial Analyst" tool, showing slope values in the study area ranging from 0 to 88.09° (Fig. 3b).

2.3.1.3. Aspect. Aspect from DEM data affects FWH by orienting slopes in relation to fog-bearing winds, with slopes facing the wind getting better moisture interception and fog exposure, enhancing collection efficiency (Schemenauer and Cereceda, 1994). In the Northern

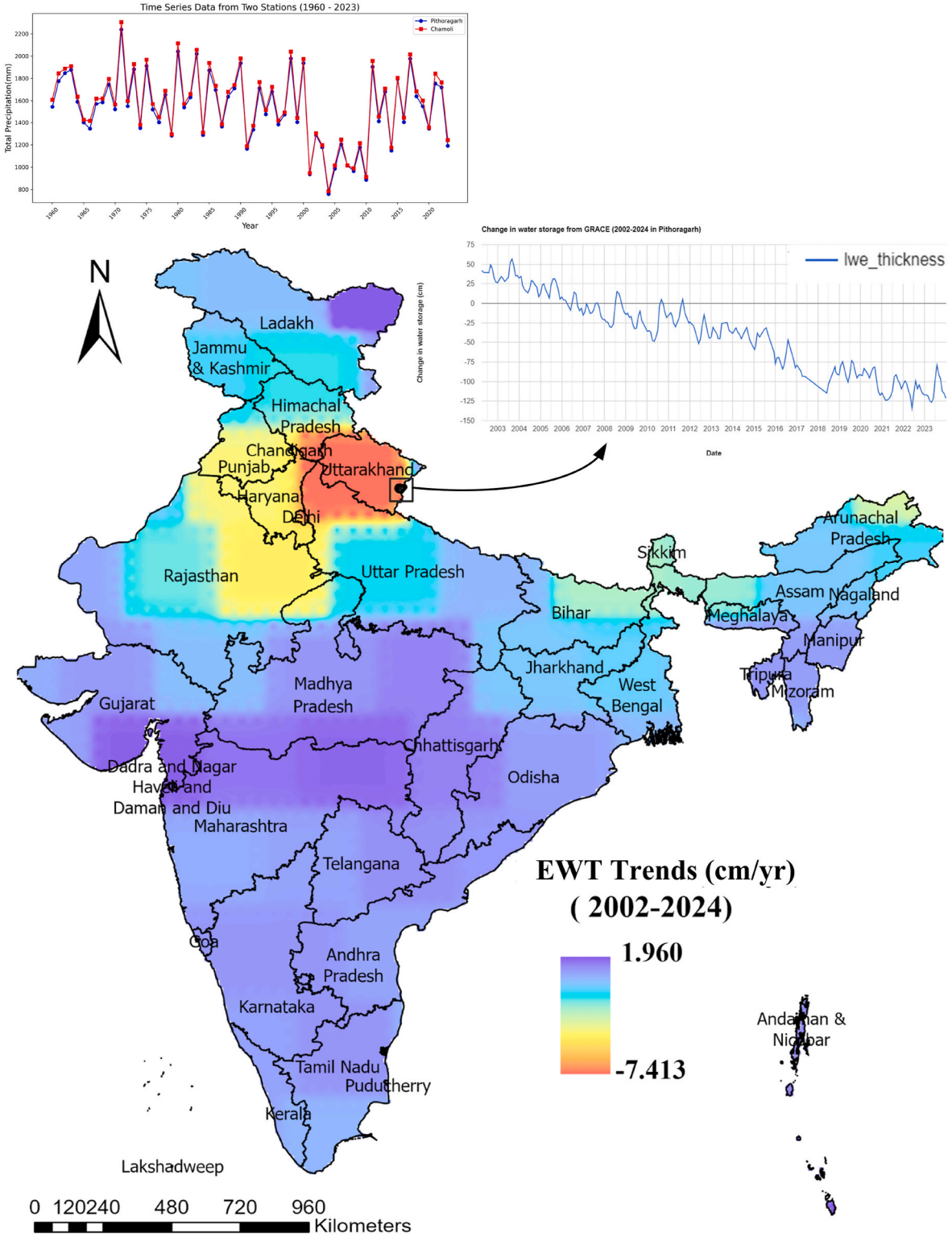

Fig. 2. Precipitation (1960–2023) and EWT (2002–2023) trends of the study area, adopted form (Sahoo et al., 2025).

Hemisphere, north-facing slopes remain cooler and retain more moisture, which promotes higher fog persistence. This aspect map was derived from the DEM using the "Aspect" tool within the "Surface" toolbox of the "Spatial Analyst extension" in ArcGIS version 10.7. The resulting map was classified into eight directional categories: north, south, east, west, northeast, southeast, northwest, and southwest (Fig. 3c).

2.3.1.4. Curvature. Curvature influences FWH by affecting airflow dynamics and moisture accumulation. Concave surfaces tend to concentrate fog moisture and enhance water collection, whereas convex surfaces promote fog dispersion and reduce potential (Agam and Berliner, 2005). The Curvature map was generated from the DEM using ArcGIS 10.7's "Curvature" tool in the "Surface" section. This map (Fig. 3d) illustrates the terrain's concavity (from −33.78 to 0) and convexity (from 0.0001 to 307.09) within the study area.

Table 1
Conditioning factors used for current and future FWH mapping.

Parameter	Conditioning subfactors	Min.	Max	Avg.	Std.	Description	Type	Source
Topographic	Elevation (m)	416	2474	1421	420	USGS/SRTMGL1_003 DEM, 30 m	Numerical	(URL:https://cmr.earthdata.nasa.gov/)
	Slope (%)	0	75.92	25.55	11.99		Numerical	
	Aspect	–	–	–	–		Categorical	
	Curvature	–	–	–	–		Categorical	
	TRI	0.111	0.888	0.494	0.08		Numerical	
	TPI	−72.33	597.33	−0.28	15.90		Numerical	
	Sky view factor (SV)	0.121	1	0.90	0.07		Numerical	
Hydro-Climatic	Precipitation (Pr) (mm)	124.63	144.19	132.13	3.23	IDAHO_EPSCOR/ TERRACLIMATE, 4638.3 m, (1960–2023)	Numerical	(URL: https://www.climatologylab.org/terraclimate)
	Maximum temperature (Tmax) (°C)	21.31	27.38	24.79	1.23		Numerical	
	Minimum temperature (Tmin) (°C)	11.93	16.10	14.08	0.89		Numerical	
	Vapour pressure (VAP) (kPa)	1.32	1.72	1.53	0.08		Numerical	
	Wind exposition index (WEI)	0.75	1.34	1.04	0.10	USGS/SRTMGL1_003 DEM, 30 m	Numerical	(URL:https://cmr.earthdata.nasa.gov/)
	Wind speed (WS) (m/s)	0.37	5.52	2.40	0.77	Global Wind Atlas at 50 m	Numerical	(URL: https://globalwindatlas.info/en/about/method)
	Mean power density (PD) (w/m2)	0.12	350.65	31.77	34.11	height, 250 m	Numerical	
	Diurnal anisotropy heating (DAH)	−0.89	0.91	0.025	0.33	USGS/SRTMGL1_003 DEM, 30 m	Numerical	(URL:https://cmr.earthdata.nasa.gov/)
	Relative Humidity (RH) (%)	53.74	61.02	58.49	0.99	NOAA/GFS0P25 (2015–2023) 27830 m,	Numerical	(URL:https://www.ncei.noaa.gov/products/weather-climate-models/global-forecast)
	Topographic wetness index (TWI)	0.01	18.50	5.65	1.68	USGS/SRTMGL1_003 DEM, 30 m	Numerical	(URL:https://cmr.earthdata.nasa.gov/)
Terrain distribution	Land Use Land Cover (LULC)	–	–	–	–	ESA WorldCover 10 m, 2021	Categorical	(URL: https://esa-worldcover.org/en)
	Land surface temperature (LST), (°C)	12.61	28.54	21.16	2.31	LANDSAT/LC08/C02/T2_L2, Landsat 8, 30 m 2021–2022 (March–May)	Numerical	(URL: https://www.usgs.gov/)
	Normalized difference vegetation index (NDVI)	−0.289	1	0.626	0.136	Sentinel-2B, 10 m, (2021–2022)	Numerical	URL: https://Sci-Hub.copernicus.eu/
	Distance to road (DistRoad) (Km)	0	2.97	0.049	0.047	Open street map, vector layer	Numerical	(URL: https://www.openstreetmap.org/)
	Distance to river (Km)	0	3.35	0.082	0.064	HydroSHEDS, river network, vector layer	Numerical	(URL: https://www.hydrosheds.org/)
	Distance to buildings (DistBuildings) (Km)	0	15.27	6.50	3.47	Open street map, Google earth, vector layer	Numerical	(URL: https://www.openstreetmap.org/)
Future climatic data	Precipitation (Pr) (mm)	NASA/GDDP-CMIP6, 27830 m, (2025–2055), (ssp245, ssp585)NorESM2-LM, EC-Earth3, MIROC6					Numerical	(URL: https://registry.opendata.aws/nex-gddp-cmip6/)
	Maximum temperature (Tmax) (°C)						Numerical	
	Minimum temperature (Tmax) (°C)						Numerical	
	Relative humidity (RH) (%)						Numerical	
	Wind Speed (WS) (m/s)						Numerical	

2.3.1.5. Terrain ruggedness index (TRI). The TRI influences FWH by affecting airflow patterns and local microclimates. Moderate terrain ruggedness can improve fog capture efficiency, whereas excessive ruggedness may reduce efficiency due to installation challenges and increased surface runoff (Fessehaye et al., 2013). TRI was calculated to assess surface roughness using the DEM in ArcGIS 10.7, utilizing the "Focal Statistics" tool under "Neighborhood" and the "Raster Calculator" under "Map Algebra"toolbox. For this study, TRI values ranged from 0.11 (maximum ruggedness) to 0.89 (minimum ruggedness) (see Fig. 3e), calculated as (Riley et al., 1999a,b):

$$TRI = \left(\frac{1}{n} \sum_{i=1}^{n} (Z_n - Z_i)^2 \right)^{0.5} \quad (1)$$

where, Z_n is the elevation of the desired pixel, Z_i is the neighbouring pixel elevation, and n refers to number of surrounding pixels, which is usually considered eight.

Topographic positional index (TPI)

TPI informs FWH by indicating a location's position in the landscape. High TPI values, found on ridges and hilltops, expose sites to fog-laden winds and enhance moisture collection, while low TPI areas like valleys may have modest fog interception (Jenness, 2006). In this study, TPI was calculated using Quantum GIS v2.18.16 as described in Eq. (2) (Chauniyal and Dutta, 2018), with values ranging from −72.33 to 597.33 m (Fig. 4f).

$$\text{TPI} = \frac{E_{pixel}}{E_{surrounding}} \quad (2)$$

where E_{pixel} is the elevation of each cell, and $E_{surrounding}$ is the average elevation of the neighbouring pixels.

2.3.1.6. Sky view factor (SV). The Sky View factor (SV) is defined as the ratio of visible sky at a point to the entire hemisphere above (Böhner and Antonić, 2009). It varies across landscapes, with higher SV areas generally experiencing less fog due to increased visibility (Olcinal, 2013). SV affects FWH by controlling sky exposure; lower SV areas (like valleys) retain fog longer, enhancing water capture, while higher SV areas facilitate faster fog dissipation (Jiao et al., 2019). The SVF is calculated as follows (Böhner and Antonić, 2009):

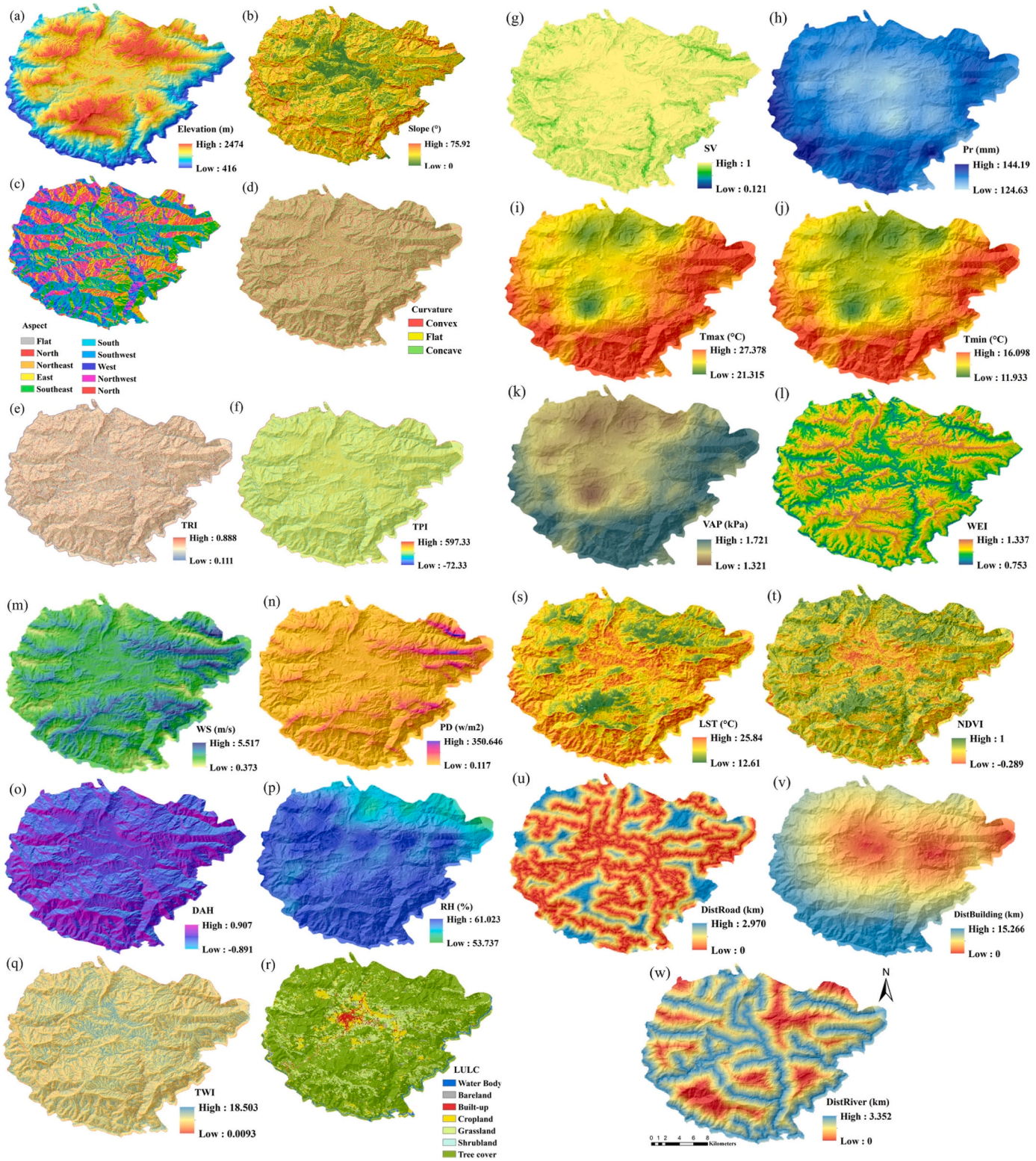

Fig. 3. FWH factors: topographical parameters: (a)–(g): (a) elevation, (b) slope, (c) aspect, (d) curvature, (e) TRI, (f) TPI and (g) sky view factor (SV); hydro-climatic parameters (h)–(p): (h) precipitation (Pr), (i) maximum temperature (Tmax), (j) minimum temperature (Tmin), (k) Vapour pressure (VAP), (l) wind exposition index (WEI), (m) wind speed (WS), (n) mean power density (PD), (o) diurnal anisotropy heating (DAH), (p) relative Humidity (RH), and (q) topographic wetness index (TWI); and Terrain distribution parameters (r)–(w): (r) land use land cover (LULC), (s) land surface temperature (LST), (t) Normalized difference vegetation index (NDVI), (u) distance to road, (v) distance to buildings and (w) distance to river.

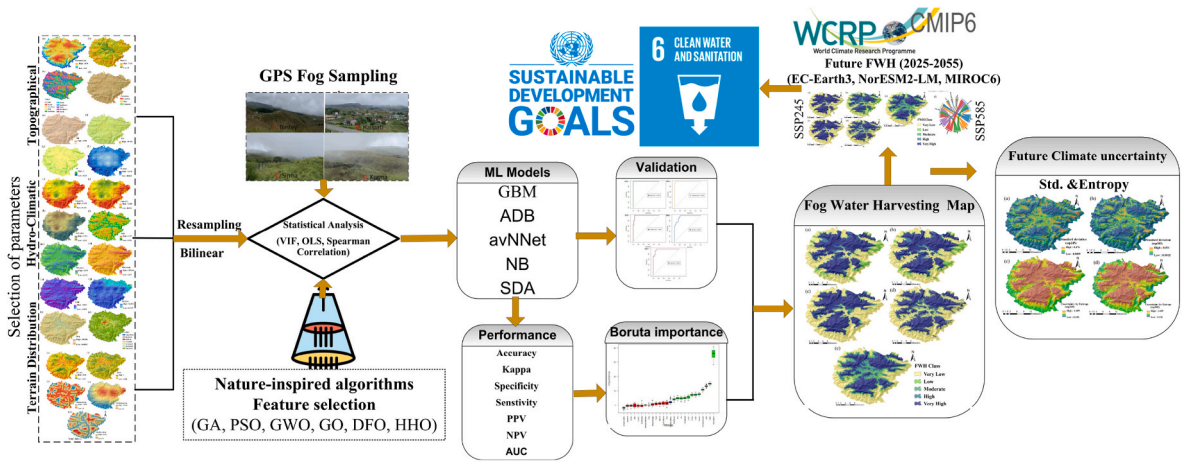

Fig. 4. Flowchart of methodology for FWH mapping.

$$SV = \frac{1}{N} \times \sum_{i=1}^{N} \left[\cos\beta.\cos^2\beta\varphi_i + \sin\beta.\cos(\phi_i - \alpha).(90 - \varphi_i - \sin\varphi_i.\cos\varphi_i)\right] \quad (3)$$

where N is the number of azimuth directions used to sample the full circle, ϕi is the horizon angle (in degrees) in the i-th direction, and ϕ_i is the corresponding azimuth angle at each point in the DEM; β represents the slope angle of the surface, while α denotes the aspect, or the azimuth of the slope's steepest descent.

For this study, the SVF was calculated using SAGA GIS (Olaf et al., 2015) by accessing the "Terrain Analysis" tools and selecting "Lighting, Visibility." SVF values range from 1, indicating unobstructed horizontal surfaces such as ridges or peaks, to 0, representing completely obstructed terrain (Böhner and Antonić, 2009). Fig. 3g presents the spatial distribution of SVF across the Pithoragarh region.

2.3.2. Hydro-climatic parameters

2.3.2.1. Precipitation (Pr). Precipitation influences FWH by increasing atmospheric humidity and surface wetness, which support fog formation. In arid regions, fog serves as a crucial supplementary water source, making fog collection systems highly relevant (Agosta et al., 2025). The annual average precipitation from 1960 to 2023 was mapped using TerraClimate datasets (https://www.climatologylab.org/terraclimate.html), which integrate WorldClim averages with CRU Ts4.0 and JRA55 data to provide fine-scale temporal information at approximately 4638-m resolution. This map was generated using the Inverse Distance Weighting (IDW) method in ArcGIS 10.7 Spatial Analyst toolbox. The western part of the study area experiences the highest annual precipitation (~144.19 mm), while the overall average across the region is 132.13 mm (Fig. 3h).

2.3.2.2. Maximum temperature (Tmax). Tmax affects FWH by influencing evaporation and fog persistence. Higher Tmax increases evaporation, reducing available fog moisture and shortening fog duration, which limits the efficiency of condensation on mesh collectors. Conversely, in cooler regions with lower Tmax, fog tends to persist longer, enhancing water collection potential (Kaseke and Wang, 2018). Annual Tmax data from 1960 to 2023 were sourced from the TerraClimate dataset (https://www.climatologylab.org/terraclimate.html) and used to generate a spatial temperature distribution map via Inverse Distance Weighting (IDW) interpolation in ArcGIS 10.7. The Tmax in the study area ranges from 21.31 °C to 27.37 °C, with an average of 24.79 °C (Fig. 3i).

2.3.2.3. Minimum temperature (Tmin). Lower Tmin values favor fog formation by enhancing nighttime cooling and limiting evaporation, thereby increasing the efficiency of fog water collection (Kaseke and Wang, 2018). A spatial Tmin map was developed using TerraClimate data (1960–2023) and interpolated with the Inverse Distance Weighting (IDW) method in ArcGIS. Tmin values in the study area range from 11.93 °C to 16.09 °C, with an average of 14.07 °C (Fig. 3j).

2.3.2.4. Vapour pressure (VAP). *VAP* reflects the atmospheric moisture content and plays a vital role in fog formation. Higher VAP levels increase the potential for condensation, thereby enhancing fog water harvesting efficiency. In contrast, lower VAP reduces the likelihood of fog development and the amount of condensable water on collection surfaces (Preetha et al., 2025). The spatial distribution of VAP across the study area was derived from TerraClimate datasets (1960–2023) using IDW interpolation. As shown in Fig. 3k, VAP values range from 1.32 kPa to 1.721 kPa, with the highest levels observed in the southern and eastern regions.

2.3.2.5. Wind exposition index (WEI). WEI measures a site's exposure to prevailing winds, affecting fog interception. Higher WEI values indicate greater exposure to moisture-laden winds, enhancing fog water collection, while lower values denote sheltered areas with less fog (Carvajal et al., 2021). Calculated using SAGA GIS Terrain Analysis, WEI is unitless, with values below 1 indicating sheltered zones and above 1 indicating wind-exposed areas (Böhner and Antonić, 2009). In this study, WEI ranges from 0.753 to 1.33 (Fig. 3l).

2.3.2.6. Wind speed (WS). WS affects FWH by influencing fog droplet movement toward collectors. Moderate winds enhance moisture capture, while high speeds can disperse fog, reducing efficiency, and low speeds may limit fog flow and collection rates (Carvajal et al., 2021). The Global Wind Atlas helps identify strong wind areas for energy production, offering free, advanced datasets. It enables users to conduct initial assessments and offers free access to downloadable datasets created using up-to-date data and advanced modeling techniques (https://globalwindatlas.info/en). WS maps at 50 m were created using these datasets via GEE (https://gee-community-catalog.org/projects/gwa/), with WS ranging from 0.37 m/s to 5.51 m/s and an average of 2.9 m/s across the study area (Fig. 3m).

2.3.2.7. Mean power density (PD). Represents the amount of wind energy available per unit area and significantly influences fog transport and concentration, impacting fog water harvesting (FWH) efficiency. Higher PD can enhance wind-driven fog movement but may reduce droplet deposition due to excessive turbulence (Khoury et al., 2023; Gandhidasan et al., 2018). In this study, PD data at 50 m were obtained

from the Global Wind Atlas for precise wind resource assessment. The eastern region exhibited the highest PD values, reaching up to 350.64 W/m^2, with an average of 31.76 W/m^2 across the study area (Fig. 3n).

2.3.2.8. Diurnal anisotropy heating (DAH). DAH describes differential land warming affecting atmospheric conditions and fog behavior. High DAH areas experience winds that disperse fog, reducing FWH efficiency, while areas with lower DAH maintain fog stability, improving collection potential (Karimidastenaei et al., 2019). DAH in QGIS is estimated using the SAGA GIS tool available in the Processing Toolbox. DAH was estimated using SAGA GIS based on Eq. (4), where its values for our study area ranged from 0.907 to −0.89 (Fig. 3o).

$$H_\alpha = \cos(\alpha_{max} - \alpha) \times \arctan(\beta) \tag{4}$$

where, α_{max} represents the aspect with the highest overall heat surplus, α denotes the slope aspect, and β indicates the slope gradient.

2.3.2.9. Relative humidity (RH). RH plays a crucial in FWH by influencing fog formation and duration. High RH levels mean the atmosphere can retain more moisture, facilitating fog formation and enhancing water condensation on collection surfaces. Near-saturation conditions (RH near 100 %) typically result in more efficient water capture. Conversely, low RH indicates drier air, reducing fog development and the effectiveness of fog harvesting systems (Bai et al., 2024). NOAA/GFS0P25 datasets from 2015 to 2023 were used to create an annual average RH map. The yearly average RH ranged from 53.73 % to 61.02 %, with a mean of 58.58 % across the study area (Fig. 3p). Higher RH values were observed in the southernmost region.

2.3.2.10. Topographic wetness index (TWI). Quantifies water accumulation based on slope and catchment area, providing insights into potential moisture distribution across a landscape (Mehravar et al., 2023). High TWI values highlight wet zones that are particularly suitable for fog water harvesting, while low values indicate drier conditions, limiting fog accumulation. TWI is computed using Equation (5) in the ArcGIS environment, based on the DEM data:

$$TWI = \ln\left(\frac{A_s}{\tan\beta}\right) \tag{5}$$

where, A_s is the catchment area, and β is the slope angle. In our study area, the maximum TWI value observed is 18.5, illustrating significant potential for moisture retention (Fig. 3q).

2.3.3. Terrain distribution parameters

2.3.3.1. Land use/land cover (LULC). LULC affects FWH by changing the landscape's ability to intercept moisture. Vegetated areas, such as forests and shrubs, enhance fog condensation, improving water collection efficiency. In contrast, urban and barren lands reduce fog capture due to limited surface roughness. The LULC map was generated by masking the ESA World Cover 2021 data with a spatial resolution of 10 m using the GEE platform (Zanaga et al., 2021). The ESA WorldCover 2021 dataset offers global land cover information at 10 m resolution using Sentinel-1 and Sentinel-2 data. It classifies LULC into 11 categories for the year 2021. This product was developed under ESA's EOEP-5 program (URL: https://esa-worldcover.org/en). The LULC classes in the study area were categorized into seven types: tree cover (71.42 %), shrubland (0.05 %), grassland (18.95 %), cropland (4.95 %), built-up (1.51 %), bare/sparse vegetation (2.14 %), and water bodies (0.97 %), (Fig. 3r; Supplementary Table 2).

2.3.3.2. Land surface temperature (LST). LST influences fog formation through moisture condensation. Lower LST values supports fog retention and improves water collection efficiency, whereas higher LST values reduces humidity and harvesting potential, making cooler surfaces ideal for fog capture. The average LST map was generated using Landsat 8 (L8) data for the period from March to May 2021–2022 (Fig. 3s). The Statistical Mono-Window (SMW) algorithm was used to estimate LST from thermal infrared satellite data through the GEE cloud platform (Ermida et al., 2020), as follows:

$$LST = a \cdot T_B + b \cdot \frac{T_B}{\epsilon} + c \tag{6}$$

where T_B is brightness temperature, ϵ is surface emissivity, and a, b, c are regression coefficients, specific to the satellite sensors and conditions. The maximum LST was around 25.84 °C in southern and central areas, with a mean LST of 21.15 °C across the study area.

2.3.3.3. Normalized vegetation index (NDVI). NDVI reflects vegetation cover, which influences local humidity, water efficiency, and microclimate stability. High NDVI facilitates moisture retention and enhances FWH effectiveness (Qiao et al., 2020), while low NDVI can hinder fog development. The 2021–2022 NDVI map was created using Sentinel-2B images via GEE (Fig. 3t), calculated from the Near Infrared (NIR) and Red bands (Huang et al., 2016):

$$NDVI = \frac{NIR - Red}{NIR + Red} \tag{7}$$

The mean NDVI value of the study area was 0.62 (Huang et al., 2016).

2.3.3.4. Distance to road (DistRoad). Distance to roads was included as a conditioning factor for FWH, as roads can alter local microclimates through heat emissions and modifications to airflow patterns, thereby hindering fog formation (Karimidastenaei et al., 2019; Baldocchi and Waller, 2014; Williams et al., 2015). We expect that areas farther from roads offer better conditions for fog formation. Road data were sourced from OpenStreetMap (OSM) and processed in ArcGIS to calculate distances, which ranged from 0 to ~2.97 km (Fig. 3u).

2.3.3.5. Distance to buildings (DistBuildings). Proximity to buildings affects airflow and fog dynamics interception, influencing FWH efficiency (Verbrugghe and Khan, 2023). Buildings can also modify local microclimates through heat retention, altered wind patterns, and the emmision of air pollutants. Thus, we expect areas farther from buildings to be more conducive to fog flow, although strategically placed structures can enhance fog capture (Caldas et al., 2018). Building data from OSM and Google Earth were used to generate a distance raster (0–15.27 km) using GIS-based spatial analysis tools (Fig. 3v).

2.3.3.6. Distance to river (DistRiver). Proximity to rivers increases local humidity levels, supporting fog formation and enhancing moisture condensation (Batisha, 2015). In this study, river network data obtained from HydroSHEDS (URL: https://www.hydrosheds.org/) were used to compute Euclidean distance layers in ArcGIS, from 0 to 3.35 km (Fig. 3w).

2.4. Methodology

The methodological framework for identifying and mapping potential FWH zones under existing and future climatic conditions consists of eight integrated phases, as illustrated in Fig. 4.

I) Parameter selection and preprocessing: A comprehensive set of geo-environmental and hydro-climatic parameters was selected, including topographical, terrain distribution, and climatic variables relevant to fog occurrence and water retention. All raster layers were resampled to a uniform spatial resolution using bilinear interpolation to ensure compatibility during analysis. II) Ground-based fog sampling: Field-based fog water sampling was conducted at strategically selected

locations (e.g., Bastey, Sirrha, Hallpat, and Kurma) using GPS devices. These ground observations served as ground-truth data for model training and validation. III) Statistical analysis: The selected variables were subjected to multicollinearity diagnostics using the following statistical tools: Variance Inflation Factor (VIF), Ordinary Least Squares (OLS) Regression, Spearman Correlation Coefficient, IV) Feature selection using nature-inspired algorithms: To identify the most influential predictors, several bio-inspired optimization techniques were applied: Genetic Algorithm (GA), Particle Swarm Optimization (PSO), Gravitational Optimization (GO), Dragonfly Optimization (DFO), Harris Hawk Optimization (HHO), and Grey Wolf Optimization (GWO), These algorithms were employed to refine the predictor set and enhance model performance. V) ML model development and FWH mapping: Five advanced MLs algorithms (GBM, ADB, avNNNet, NB and SDA) were deployed to model FWH potential. Based on the best-performing models, spatial maps were generated to classify the landscape into FWH potential zones, categorized as very low, low, moderate, high, and very high. VI) Model evaluation and validation: Model performance was assessed using a suite of evaluation metrics under 10-fold cross validation, ensuring the robustness and generalizability of model predictions. VII) Feature importance assessment: The Boruta algorithm was used to determine the relative importance of input features, facilitating further interpretation of key environmental and climatic drivers influencing FWH potential. VIII) Climate change scenario integration and uncertainty analysis: To project future FWH potential (2025–2055), outputs from CMIP6 climate models (EC-Earth3, NorESM2-LM, MIROC6) under two Shared Socioeconomic Pathways (SSPs), SSP2-4.5 and SSP5-8.5 were integrated. Standard deviation (Std.) and entropy analyses were then conducted to quantify model uncertainty and variability in FWH predictions under changing climate scenarios, enabling robust planning and adaptation strategies.

2.4.1. Statistical analysis

The statistical significance of independent variables related to fog water potential was assessed using the OLS method (Lee et al., 2022). Pearson correlation was applied to examine spatial relationships among predictors. Multicollinearity was evaluated using the Variation Inflation Factor (VIF) (Eq. , where values ≤ 10 indicate low multicollinearity and acceptable model optimization (Kim, 2019; Holloway et al., 2017; Moghimi et al., 2024).

$$VIF = \frac{1}{\text{Tolerance}} \tag{8}$$

$$\text{Tolerance} = 1 - X_j^2 \tag{9}$$

where, X_j^2 represents the coefficient of determination of the j^{th}explanatory variable regressed on all other independent variables.

2.4.2. Feature selection

To identify the most relevant predictors of fog water occurrences, feature selection was performed using six nature-inspired wrapper algorithms, inclucing GA, PSO, GO, DFO, HHO, and GWO. Each algorithm was paired with a LightGBM model, which served as the core evaluator during the optimization process. These wrappers aimed to identify the optimal subset of features by maximizing model performance through their respective fitness functions.

2.4.3. Machine learning (ML) models

To identify fog-prone areas, five ML models were employed, each offering unique advantages for spatial prediction, as summarized in Table 2. The models were implemented using the *caretEnsemble* package within the R software environment. Comprehensive information on the required R packages and tuning parameters was provided in Supplementary Table 3 and illustrated in Supplementary Fig. 1.

Table 2
Overview of ML models used for mapping FWH potential mapping.

Model	Definition	strength
Gradient boosting machine (GBM)	An ensemble method that builds sequential decision trees, each one improving on the errors of the previous, to enhance model accuracy (Friedman, 2001; Natekin and Knoll, 2013; Singha et al., 2025).	High accuracy and robustness against overfitting (with proper tuning); handles missing data; scalable for large, high-resolution datasets.
Adaptive Boosting (ADB)	A boosting technique that combines multiple weak classifiers, giving more weight to previously misclassified instances to improve overall performance (Sun et al., 2011; Singha et al., 2025).	Effective in handling imbalanced and binary classification tasks; simple implementation; reliable with minimal tuning.
Model Averaged Neural Network (avNNet)	An ensemble of feed-forward neural networks with different random initializations, averaged to improve prediction stability (Ripley, 1996, 2007; Singha et al., 2025).	Capable of modeling complex, non-linear relationships; uses weight decay and hidden layer settings to prevent overfitting and enhance generalization.
Naive Bayes (NB)	A probabilistic classifier based on Bayes' theorem, assuming conditional independence between features (Rish, 2001).	Computationally efficient; performs well with high-dimensional data; minimal training required; effective when feature independence is approximately valid.
Shrinkage Discriminant Analysis (SDA)	An extension of linear discriminant analysis that applies shrinkage to stabilize covariance estimation in high-dimensional data (Zuber and Strimmer, 2009).	Manages multicollinearity and overfitting; enhances variable selection through shrinkage; well-suited for noisy or complex environmental datasets.

2.5. Future trends of FWH

This study evaluated future trends in FWH potential using the NEX-GDDP-CMIP6 dataset, which provides high-resolution (0.25°) downscaled climate projections derived from CMIP6 General Circulation Models (GCMs) (Thrasher et al., 2012; URL: https://cds.climate.copernicus.eu). The dataset incorporates climate scenarios based on Shared Socioeconomic Pathways (SSPs), specifically SSP2-4.5 (moderate emissions) and SSP5-8.5 (high emissions), allowing the assessment of potential changes in FWH under different climate trajectories. To address uncertainties associated with individual GCMs, a multi-model ensemble approach was employed by integrating outputs from three well-validated models: EC-Earth3, NorESM2-LM, and MIROC6 (Lybarger et al., 2024; Singha et al., 2024; Cui et al., 2021; see Supplementary Table 4).

Key climate variables relevant to fog formation, including annual averages of precipitation (Pr), maximum and minimum temperature (Tmax, Tmin), wind speed (WS), and relative humidity (RH), were extracted for the period 2025–2055 (see Supplementary Figure.2 and Figure.3). These variables served as inputs for modeling FWH potential and assessing the influence of future climate change on fog occurrence. Furthermore, they provide essential context for broader climate impact and hydrological analyses relevant to FWH systems (Siabi et al., 2023).

2.6. Validation metrics

Model performance was evaluated using a 70:30 train–test split, with 140 plots allocated for training and 60 plots reserved for testing. To enhance model generalization and minimize overfitting, 10-fold cross-validation was also employed (Guan and Burton, 2022).

Model validation was conducted using standard performance metrics, including accuracy, Kappa coefficient, sensitivity, specificity, pos-

itive predictive value (PPV), negative predictive value (NPV), and F1-score, as defined in Eq. (10)–(16):

$$\text{Accuracy} = \frac{\text{TP} + \text{TN}}{\text{TP} + \text{TN} + \text{FP} + \text{FN}} \tag{10}$$

$$\text{Kappa coefficient} = \frac{P_{\text{obs}} - P_{\text{exp}}}{1 - P_{\text{exp}}} \tag{11}$$

$$\text{Sensitivity} = \frac{\text{TP}}{\text{TP} + \text{FN}} \tag{12}$$

$$\text{Specificity} = \frac{\text{TN}}{\text{TN} + \text{FP}} \tag{13}$$

$$PPV = \frac{\text{TP}}{\text{TP} + \text{FP}} \tag{14}$$

$$NPV = \frac{\text{TN}}{\text{TN} + \text{FN}} \tag{15}$$

$$\text{F1} - \text{score} = 2 \times \frac{\text{PPV} \times \text{Sensitivity}}{\text{PPV} + \text{Sensitivity}} \tag{16}$$

where, TP represents true positive, TN denotes true negative, FP false positives, and FN false negatives. P_{obs} denotes the observed proportion of positive cases, and P_{exp} is the expected proportion of positive cases under random chance.

This study also employed the Boruta wrapper algorithm (Kursa and Rudnicki, 2010) to evaluate the relative importance and sensitivity of parameters influencing FWH potential. The Boruta algorithm applies a z-score–based criterion to assess the significance of each feature by comparing its importance with that of randomized shadow features. The selected parameters were subsequently analyzed using statistical techniques to quantify their sensitivity and contribution to variations in FWH potential occurrences.

To investigate uncertainty in projected future FWH trends, an ensemble modeling approach was employed by combining outputs from multiple climate and ML models. Pixel-wise standard deviation and entropy analyses were conducted to quantify the spatial variability and uncertainty across ensemble predictions (Schneider, 2025; Chapman, 1986). The standard deviation metric measures the degree of variability in fog probability estimates across models for each pixel, while entropy (Eq. (17)) captures uncertainty based on the distribution of predicted probabilities.

$$H(p) = -\sum_{i=1}^{n} p_i \log_2 (p_i) \tag{17}$$

where p_i is the fog probability from the i-th model, and, n is the total number of models. Higher entropy and standard deviation indicate greater model disagreement, while lower values suggest stronger consensus and more reliable predictions.

3. Results

3.1. Statistical OLS and multicollinearity analysis

The Spearman correlation analysis, depicted in Fig. 5, revealed several significant relationships between FWH potential and various environmental variables. FWH potential exhibited a strong positive correlation with elevation (0.86), indicating the importance of altitudes in fog formation. Other positive correlations included the WEI (0.62), PD (0.52), WS (0.55), and SV (0.37), highlighting the influence of atmospheric and topographic conditions on fog formation. Conversely, FWH potential demonstrated negative correlations with Tmax, Tmin, LST, DistRoad, DistBuildings, VAP, and Pr. These negative correlations

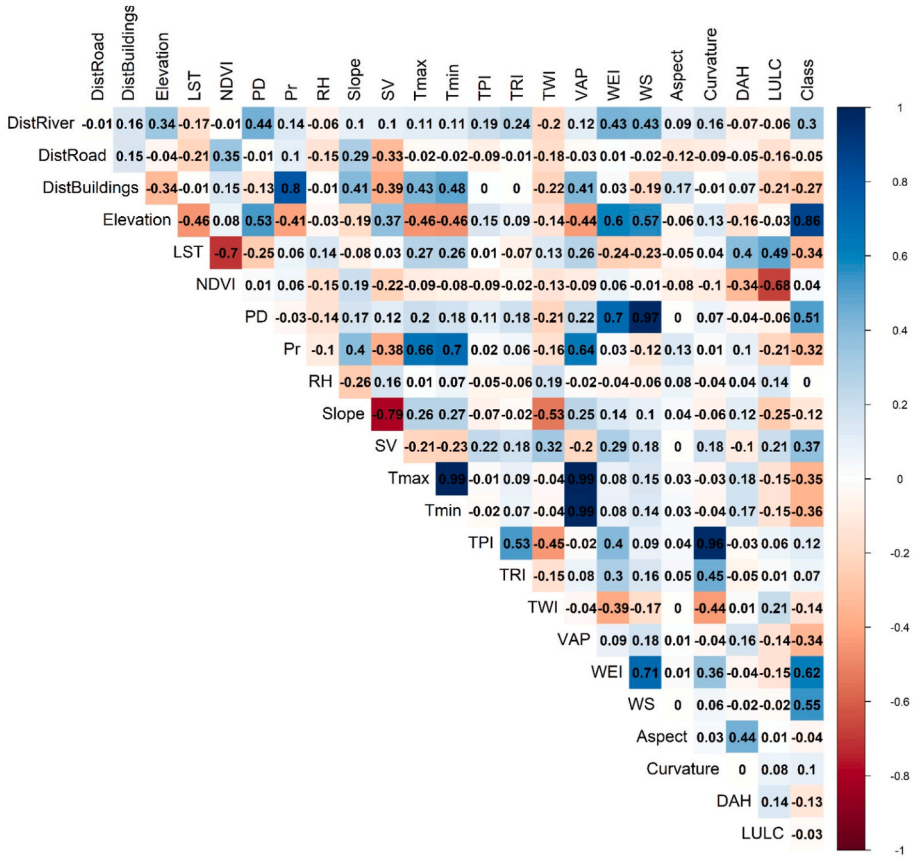

Fig. 5. Spearman correlation analysis of conditioning parameters for FWH.

suggest that higher temperatures and close proximity to urban infrastructures adversely affect fog formation, possibly through heat island effects and microclimatic disturbances. DistBuildings was strongly positively correlated with PD (0.85) and LST (0.53), reflecting the impact of urban areas on local heat retention and energy usage. Elevation was negatively correlated with LST (−0.70), but positively correlated with power density (0.53) and NDVI (0.48), indicating the characteristics of cooler and vegetated highlands. LST also showed positive associations with NDVI (0.50) and PD (0.51), further emphasizing urban influence on surface temperature dynamics. Tmax and Tmin were highly correlated (0.99), reflecting stable diurnal temperature patterns within the study area. Additional notable relationships included slope with SV (0.79), TWI with VAP (0.90), and VAP with WEI (0.71), emphasizing the interconnected roles of terrain morphology and atmospheric moisture in influencing FWH potential.

The OLS analysis in Table 3, showed that elevation, RH, and WEI were statistically significant predictors ($p < 0.001$), with Tmin also significant at the 95 % confidence level. The coefficient range varied from −0.730 (TRI) to 2.182 (WEI), and the model's R^2 (0.709), F statistic (12.20), and Prob > chi2 (0.578) indicated a good overall model fit. The Durbin-Watson statistic (~1.981) suggested moderate autocorrelation.

Multicollinearity diagnostics using the VIF confirmed that all variables were within acceptable limits (VIF ≤10), indicating no serious multicollinearity issues. VIF values ranged from 1.314 (curvature) to 6.913 (Pr), with tolerance values from 0.145 to 0.736 (see Table 3).

3.2. Metaheuristic feature selection analysis

In this section, the performance of considered metaheuristic algorithms was evaluated for feature selection in FWH site suitability modelling. The objective function values indicated that GA yielded the highest precision (0.0008), followed by HHO (0.0007), GO (0.0007), DFO (0.0006), PSO (0.0005), and GWO (0.0001), respectively (Fig. 6a–f). The results of the feature selection process revealed that key variables such as elevation, WS, WEI, VAP, DAH, RH, PD, Tmax, Tmin, and SV are the most influential in determining FWH site suitability (Supplementary Table 5).

3.3. Spatial FWH analysis

FWH was classified into five categories ranging from very low to very high using the Natural Breaks method within the ArcGIS platform (Jenks, 1967). This data-driven method minimizes within-class variance and maximizes between-class differences, making it ideal for clearly representing non-uniform spatial patterns in environmental studies like fog water potential (Gohil et al., 2024; Singh et al., 2025).

Fig. 7a–e showed the FWH maps generated using GBM, ADB, avNNet, NB, and SDA models. These ML models predicted the extent of each fog water potential class, as detailed in Table 4. The GBM model identified the largest area for the very high fog water potential class, accounting for approximately 43.91 % (214.84 km^2), and for the very low potential class, accounting for about 37.61 % (184.03 km^2).

In ADB, the coverage in terms of very-high, high, moderate, low, and very-low potentiality classes is 43.84 % (214.48 km^2), 6.03 % (29.50 km^2), 2.08 % (10.16 km^2), 9.24 % (45.19 km^2), and 38.82 % (189.94 km^2), respectively. The avNNet model estimated that 44.90 % (219.66 km^2) of the study area has a very low potentiality. The low and moderate potential zones covered 3.06 % (14.95 km^2) and 3.21 % (15.70 km^2) of the area, respectively (Table 3), while the remaining 48.84 % (238.96 km^2) fall into the high to very high fog water potential class. The fog water potential map created by the SDA model indicated that 167.11 km^2 (34.16 %) of the study area has a very high fog water potential zone. The low and very-low fog water potential classes accounted for 9.53 % and 33.50 % of the study area, respectively. The moderate potentiality class covered 48.82 km^2 (9.98 %) of the area. According to the NB model, the study area has 42.97 % (210.25 km^2) in the very-high fog water potentiality class, followed by 4.35 % (21.29 km^2) in the high potential class, 3.45 % (16.87 km^2) in the moderate potential class, 4.32 % (21.13 km^2) in the low, and 219.73 km^2 (44.91 %) in the very-low fog water potential classes, respectively (Table 4). In general, the ML models showed a trend where the central part of the study area has a higher concentration of fog potential zones, which gradually reduced towards the outskirts of the study area.

3.4. Validation

The validation results presented in Table 5 and Fig. 8 indicate that among the tested ML models, ADB and GBM demonstrated the highest

Table 3
OLS and VIF analysis results for fog water potentiality parameters.

Parameter	Tolerance	VIF	β	Std. err	t	P>|t|
DistRiver	0.614	1.629	−0.076	0.001	−1.435	0.154
DistRoad	0.722	1.385	0.096	0.001	1.517	0.132
DistBuildings	0.296	3.384	0.025	0.001	0.161	0.872
Elevation	0.195	5.139	0.001	0.001	4.548	0.00***
LST	0.230	4.357	0.040	0.025	1.624	0.107
NDVI	0.245	4.089	0.094	0.484	0.195	0.846
PD	0.161	6.207	−0.001	0.001	−0.320	0.749
Pr	0.145	6.913	0.019	0.021	0.945	0.347
RH	0.283	3.529	0.889	0.39	3.78	0.00***
Slope	0.163	6.117	0.001	0.002	0.354	0.724
SV	0.173	5.789	0.671	0.868	0.772	0.442
Tmax	0.620	2.636	0.044	0.038	1.159	0.249
Tmin	0.436	3.103	−0.014	0.01	−2.71	0.01**
TPI	0.601	2.748	−0.025	0.026	−0.956	0.341
TRI	0.607	1.648	−0.730	0.518	−1.408	0.162
TWI	0.490	2.041	0.013	0.020	0.673	0.502
VAP	0.396	3.202	−0.001	0.003	−0.169	0.866
WEI	0.195	5.139	2.182	0.543	4.018	0.00***
WS	0.635	2.448	−0.001	0.099	−0.007	0.994
Aspect	0.634	1.578	0.010	0.014	0.727	0.469
Curvature	0.736	1.314	0.036	0.062	0.576	0.566
DAH	0.584	1.713	−0.012	0.102	−0.118	0.906
LULC	0.443	2.259	−0.003	0.003	−0.765	0.446
	R-squared = 0.709		F-statistic = 12.20	DurbinWatson = 1.981	Prob > chi2 = 0.578	

β ~Coefficient; t ~ *t*-test std err ~ Standard error, Robust standard errors~ *p < 0.05, **p < 0.01, and, ***p < 0.001,F ~ Statistical, R2~ Linear regression.

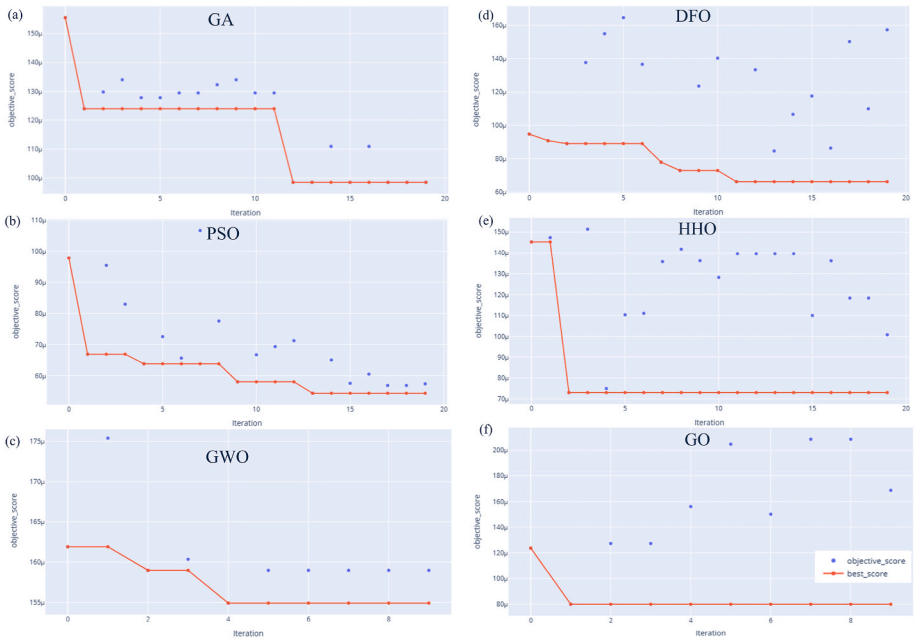

Fig. 6. Convergence trends of the best objective function values across iterations for various nature-inspired optimization algorithms: (a) GA, (b) PSO, (c) GWO, (d) DFO, (e) HHO, and (f) GO.

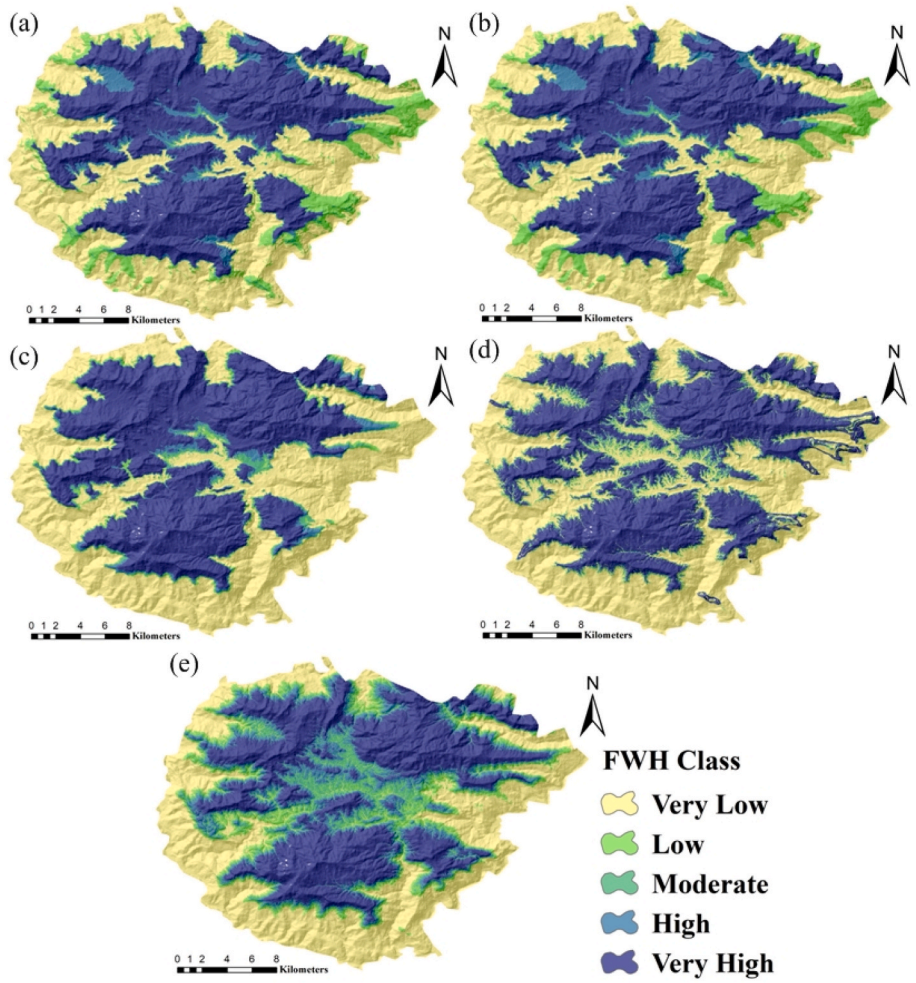

Fig. 7. Predicted FWH distribution map through ML models; (a) GBM model, (b) ADB model, (c) avNNet model, (d) NB model, and (e) SDA model.

Table 4
Areal coverage of fog water potential classes of ML models.

Model	GBM		ADB		avNNet		NB		SDA	
Class	Area		Area		Area		Area		Area	
	(km2)	(%)	(km2)	(%)	(km2)	(%)	(km2)	(%)	(km2)	(%)
Very Low	184	37.6	190	38.8	220	44.9	220	44.9	169	34.5
Low	48.7	9.96	45.2	9.24	15	3.06	21.1	4.32	46.7	9.53
Moderate	11.7	2.4	10.2	2.08	15.7	3.21	16.9	3.45	48.8	9.98
High	30	6.12	29.5	6.03	19.8	4.05	21.3	4.35	57.9	11.8
Very high	215	43.9	214	43.8	219	44.8	210	43	167	34.2

Table 5
Validation results produced by ML models in FWH mapping.

Model	Accuracy	Kappa	Sensitivity	Specificity	PPV	NPV	F1 Score	AUC
GBM	0.967	0.933	0.933	1.000	1.000	0.938	0.966	0.999
ADB	0.983	0.967	0.967	1.000	1.000	0.967	0.983	0.999
avNNet	0.900	0.800	0.867	0.933	0.929	0.875	0.897	0.967
NB	0.883	0.767	0.833	0.933	0.926	0.849	0.877	0.941
SDA	0.933	0.867	0.933	0.933	0.933	0.933	0.933	0.967

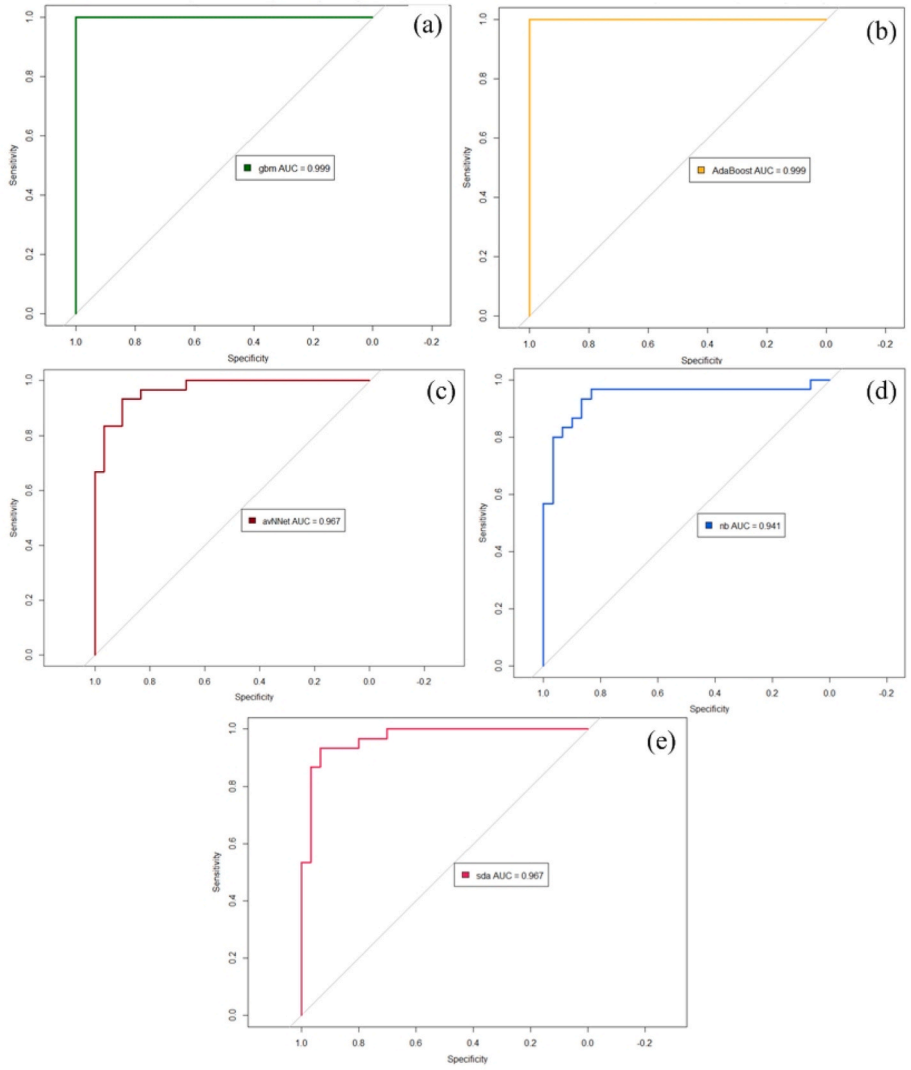

Fig. 8. AUROC analysis of the ML models: (a) GBM, (b) ADB, (c) avNNet, (d) NB, and (e) SDA models.

predictive performance for FWH mapping. ADB achieved the best overall results, with the highest accuracy (0.983), Kappa (0.967), sensitivity (0.967), F1 score (0.983), and a perfect score for specificity and PPV, around 1. Its AUC also reached 0.999, confirming its excellent classification capability (see Fig. 8). Similarly, GBM showed outstanding performance, with an accuracy of 0.967, sensitivity of 0.933, and specificity and PPV around 1.000. Its F1 score (0.966) and AUC (0.999) further affirm its robustness and reliability for mapping suitable fog water harvesting zones (see Fig. 8). In the moderate performance category, the SDA model with F1 score of 0.933, with an AUC of 0.967 maintained a balanced and consistent result across all metrics. These values suggest that SDA can serve as a reliable model, especially in applications where interpretability is important alongside accuracy. Conversely, NB and avNNet models demonstrated comparatively lower performance. NB recorded the lowest values across multiple metrics, including accuracy (0.883), Kappa (0.767), sensitivity (0.833), and F1 score (0.877), although its specificity (0.933) and PPV (0.926) were relatively high. The avNNet model showed slightly better performance than NB, with an accuracy of 0.900 and F1 score of 0.897, but still fell behind the top-performing models.

3.5. Sensitivity analysis

Sensitivity analysis using the Random Forest-based Boruta algorithm identified the most influential factors contributing to FWH within the study area (Table 6). Elevation emerged as the most critical parameter (mean importance: 35.31), followed by WEI (14.92), WS (13.24), PD (10.78), and Tmax (7.70). Variables such as VAP, Tmin, LST, DistBuildings, SV, Pr, and DistRiver showed moderate importance (Fig. 9). In contrast, factors including curvature, NDVI, TWI, slope angle, TRI, distance to road, RH, LULC, DAH, and aspect were comparatively less influential in the model. It is noteworthy that Certain variables, such as Tmin, were found to be statistically significant in the OLS regression ($p < 0.05$), yet were considered only moderately important in the Boruta analysis. This contrast reflects fundamental differences between the two approaches. OLS highlights linear associations under specific assumptions, whereas Boruta evaluates each variable's unique contribution to predictive accuracy within a nonlinear, interaction-sensitive framework. Variables with shared variance (e.g., Tmin, Tmax, RH) may appear more or less important depending on the modeling context and redundancy effects.

3.6. GRACE analysis

To estimate EWT, the study utilized GRACE products provided by the Centre for Space Research (CSR) and the Jet Propulsion Laboratory (JPL) for the study area, as shown in Fig. 10(a) and (b). Heat maps derived from these datasets revealed historically abundant water availability from August to November (2002–2011). However, a declining trend in EWT has emerged in recent years, particularly from January to September (2016–2022) (see Fig. 10).

The regional water balance has shown shallow levels, dipping below −60 cm in the most recent years (2021–2022). In light of anticipated climate change impacts, FWH has been proposed as a viable solution to mitigate water shortages in regions with insufficient rainfall and baseline water resources.

3.7. Future FWH mapping

To assess future climate impacts on FWH, the study employed CMIP6 projections for 2025–2055 using EC-Earth3, NorESM2-LM, and MIROC6 models. Key variables (Pr, Tmax, Tmin, RH, and WS) were analyzed under SSP2-4.5 and SSP5-8.5 scenarios (see Supplementary Figs. 2 and 3). ML models were then applied to map spatial FWH potential across both scenarios (Fig. 11a–e and 12a–12e).

Under SSP2-4.5, the "Very High" class coverage was highest with avNNet (49.24 %), followed by GBM (43.15 %) and NB (42.09 %). The "Very Low" class also had substantial coverage, with avNNet at 46.44 %, NB at 39.93 %, and GBM at 38.96 %. The "Low" class ranged from 1.33 % (avNNet) to 15.53 % (ADB) and "Moderate" areas were least seen in avNNet (0.98 %) and GBM (2.14 %). For the "High" class, SDA (12.61 %) and ADB (15.10 %) predicted higher values. The ensemble mean coverage was 20 %, with avNNet exhibiting the greatest spatial variability (Std. 22.75 %).

Fig. 12(a–e) illustrate variations in FWH classes predicted by different models under the SSP5-8.5 scenario. The "Very High" class was most extensive, with avNNet (51.27 %) and GBM (51.32 %) leading, followed by NB (41.85 %) (Fig. 12f), showing these models identify large areas suitable for FWH under extreme conditions. The "Very Low" class also had significant presence in avNNet (46.21 %), NB (40.16 %), and GBM (42.33 %), indicating model divergence in low potential zones.

"Low" and "Moderate" classes were more limited, with "Low" ranging from 0.82 % (avNNet) to 11.65 % (ADB), and "Moderate" peaking at 10.54 % in SDA. The "High" class showed intermediate coverage, with

Table 6
Importance of fog water potential variables by Boruta algorithm.

Parameter	meanImp	medianImp	minImp	maxImp	normHits	decision
Elevation	35.31	36.28	28.09	40.72	1.00	Confirmed
WEI	14.92	14.95	13.44	16.25	1.00	Confirmed
WS	13.24	13.20	11.99	14.56	1.00	Confirmed
PD	10.78	10.80	9.25	12.09	1.00	Confirmed
Tmax	7.70	7.72	6.60	8.84	1.00	Confirmed
VAP	7.33	7.21	5.74	9.07	1.00	Confirmed
Tmin	7.14	7.15	5.95	8.54	1.00	Confirmed
LST	5.59	5.63	3.34	7.23	0.98	Confirmed
DistBuildings	4.97	5.06	2.29	6.55	0.97	Confirmed
SV	4.84	4.82	3.05	6.71	0.97	Confirmed
Pr	4.74	4.84	2.50	6.13	0.95	Confirmed
DistRiver	4.12	4.14	1.90	6.35	0.88	Confirmed
TPI	1.42	1.53	−1.94	3.49	0.06	Rejected
Curvature	1.33	1.31	−0.87	2.96	0.29	Rejected
NDVI	1.11	1.26	−1.09	2.44	0.12	Rejected
TWI	1.00	1.03	−0.53	2.40	0.02	Rejected
Slope	0.62	0.41	−1.28	3.43	0.05	Rejected
TRI	0.11	0.05	−0.84	1.73	0.00	Rejected
DistRoad	−0.22	−0.35	−1.37	3.02	0.02	Rejected
RH	−0.26	−0.56	−2.20	1.92	0.00	Rejected
LULC	−0.52	−0.35	−1.99	0.85	0.00	Rejected
DAH	−0.61	−0.64	−2.61	0.71	0.00	Rejected
Aspect	−0.70	−0.70	−3.00	0.83	0.00	Rejected

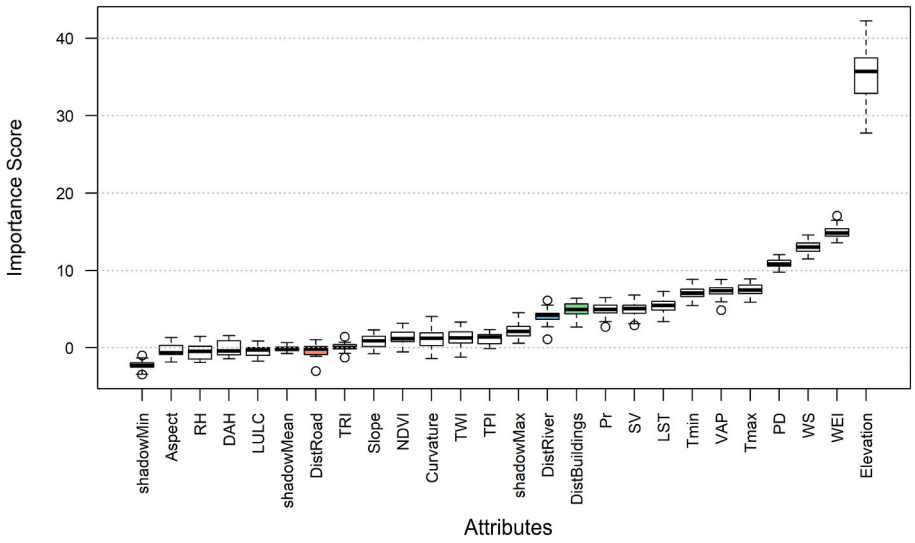

Fig. 9. Boruta algorithm-based fog water conditioning parameters analysis.

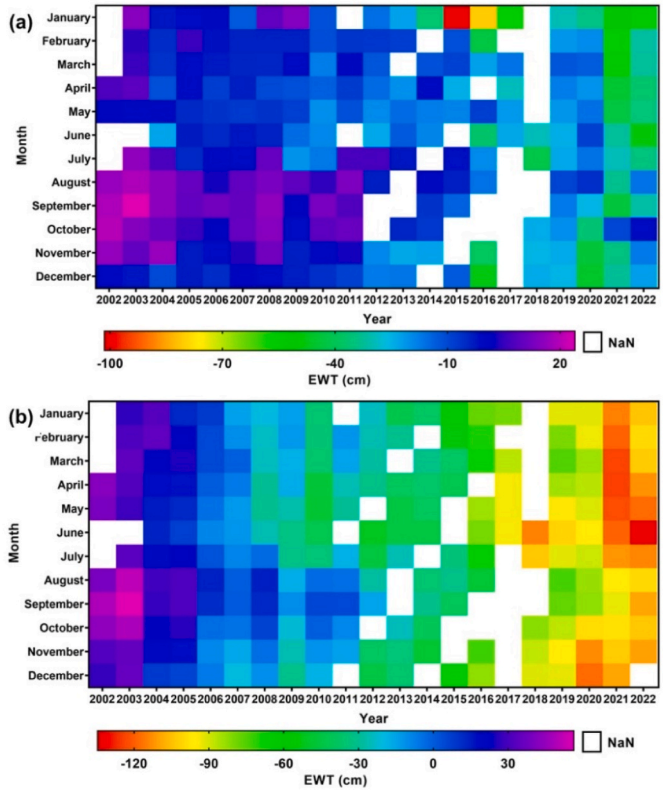

Fig. 10. Monthly variation in EWT from 2002 to 2022 within the study area, as derived from GRACE datasets: (a) CSR, and (b) JPL products.

ADB (15.74 %) and SDA (11.97 %) estimating higher shares (Fig. 12b & e). In this scenario also the ensemble average across all models remained at 20 %. Variability was notable, with avNNet showing the highest standard deviation (23.52 %), followed by GBM (22.10 %), reflecting spatial heterogeneity.

Spatial uncertainty in FWH potential under SSP2-4.5 and SSP5-8.5 scenarios was assessed using standard deviation and entropy analysis (Fig. 13a–d). Fig. 13a and b shows standard deviation values for FWH suitability across models: under SSP2-4.5, values range from 0.0009 to 0.476, indicating low disagreement except in ridgelines and elevated areas, while SSP5-8.5 shows increased variability (0.0015–0.501), reflecting broader model predictions under extreme conditions.

Entropy-based maps (Fig. 13c and d) add a probabilistic perspective—SSP2-4.5's entropy ranges from 0.156 to 1.609, with higher uncertainty in central and western regions, while SSP5-8.5 extends from 0.126 to 1.609, revealing central region uncertainty but more model agreement in peripheral zones. These results emphasize the greater predictive uncertainty in complex topographies, especially under SSP5-8.5, highlighting the importance of ensemble and uncertainty quantification for resilient FWH planning in future climate scenarios.

4. Discussion and conclusion

This study presented a comprehensive ML-based assessment of FWH potential in the Pithoragarh district of Uttarakhand, incorporating 23 geo-environmental variables and future climate scenarios. Statistical analyses, including correlation, OLS, VIF, and ML-based Boruta analysis revealed that topographic and atmospheric conditions are the dominant factors influencing FWH suitability across the study area. Among these, elevation, WEI, and WS emerged as the most influential predictors, aligning with established physical mechanisms of fog formation in mountainous areas (Pilié et al., 1975; Pu et al., 2023).

Distribution maps from the best-performing ML models (ADB and GBM) showed that mountainous regions exhibited greater FWH potential due to favorable conditions such as lower temperatures, orographic uplift, and terrain-driven airflow. These findings are consistent with the concept of upslope fog, wherein moist air masses ascend and cool adiabatically, resulting in condensation (Khoury et al., 2023). Conversely, urban areas with extensive infrastructure and anthropogenic heat emissions demonstrated reduced fog potential, corroborating prior findings on the negative impact of land modification on fog formation (Lange et al., 2003; Keim-Vera et al., 2024). OLS diagnostics confirmed the reliability of the predictors. The highest FWH potential was linked to slopes between 26.27° and 52.51°, consistent with Pretorius (2009), who emphasized slope's role in intercepting fog-bearing winds. However, the influence of elevation is more nuanced, as it varies depending on regional topographic context and fog type, as highlighted by Keim-Vera et al. (2024). These observations underscore the need for region-specific interpretations in data-driven modeling.

The Boruta algorithm further validated the importance of key predictors. Although features such as curvature, NDVI, and TWI demonstrated moderate importance, their physical relevance to fog formation remains context-dependent. For instance, NDVI might inversely correlate with fog occurrence due to enhanced surface turbulence in

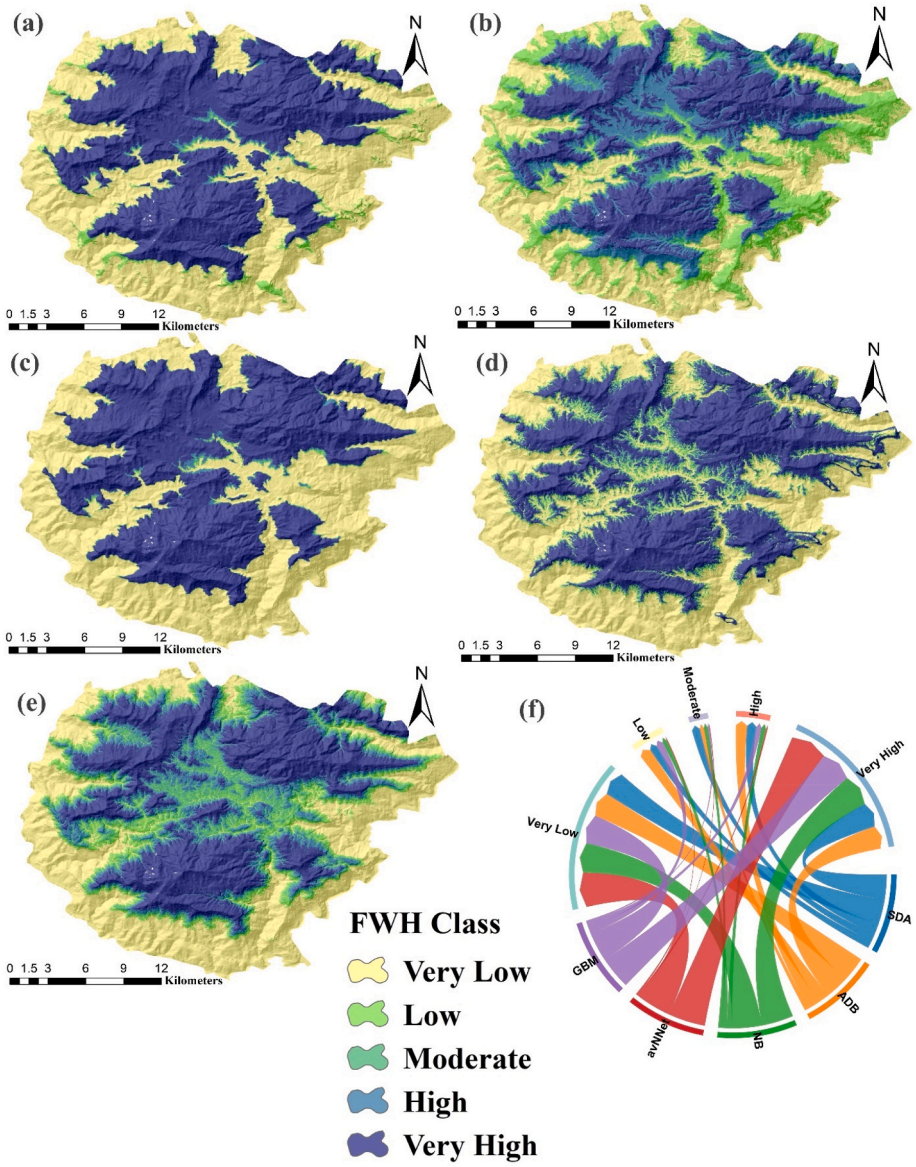

Fig. 11. Future FWH potential maps and area coverage for SSP2-4.5 scenario (a) GBM model, (b) ADB model, (c) avNNet model, (d) NB model, and (e) SDA model and (f) chord diagram for area coverage.

vegetated areas, whereas TWI is more related to surface hydrology and may not fully capture airborne moisture dynamics.

Among the ML models applied, ADB and GBM achieved the highest predictive accuracy for identifying suitable FWH sites, with F1 scores exceeding 0.966 and AUC values approaching 0.999. Although, these results have been achived on a few test data, they underscore the effectiveness of ensemble learning techniques in capturing the complex, nonlinear interactions among geo-environmental variables that influence fog formation and collection potential. In contrast, models such as SDA performed moderately, while avNNet and NB showed limited reliability, making them less suitable for high-precision mapping of fog-prone areas. The most reliable FWH suitability maps, produced by ADB and GBM, identified very high potential zones covering over 43 % of the study area, mainly in the northern and central mountainous regions. This central clustering is driven by topographic and thermal factors: upslope fog forms as moist air cools during ascent, while valley fog results from cold air pooling in low basins under clear nighttime skies. These processes together explain the region's high FWH potential (Khoury et al., 2023; Pilié et al., 1975).

Projections under CMIP6 scenarios (SSP2-4.5 and SSP5-8.5) showed spatial variability across models. GBM and avNNet predicted broader extents of "very high" potential zones, albeit with greater uncertainty under extreme scenarios. In contrast, ADB and SDA offered more conservative yet spatially consistent outputs. The ensemble mean remained stable (~20 %), reducing individual model biases. Future hotspots were consistently located in the north-central region, though model disagreement increased under SSP5-8.5, especially in areas with complex topography. These findings highlight the importance of ensemble and uncertainty-aware modeling for long-term FWH planning.

A key strength of this approach, aligned with Karimidastenaei et al. (2019) , lies in leveraging predictive variables such as hydro-climatological, topographic, and LULC features for data-driven suitability mapping. However, it is important to acknowledge the limitations of the current models. Prediction accuracy is inherently dependent on the quality and resolution of input data (e.g., LST, precipitation, wind speed, humidity). Temporal gaps or inconsistencies in data collection can introduce uncertainty. Hence, regular updates of FWH suitability maps are essential to reflect evolving climatic and environmental conditions.

From an implementation standpoint, fog collection infrastructure,

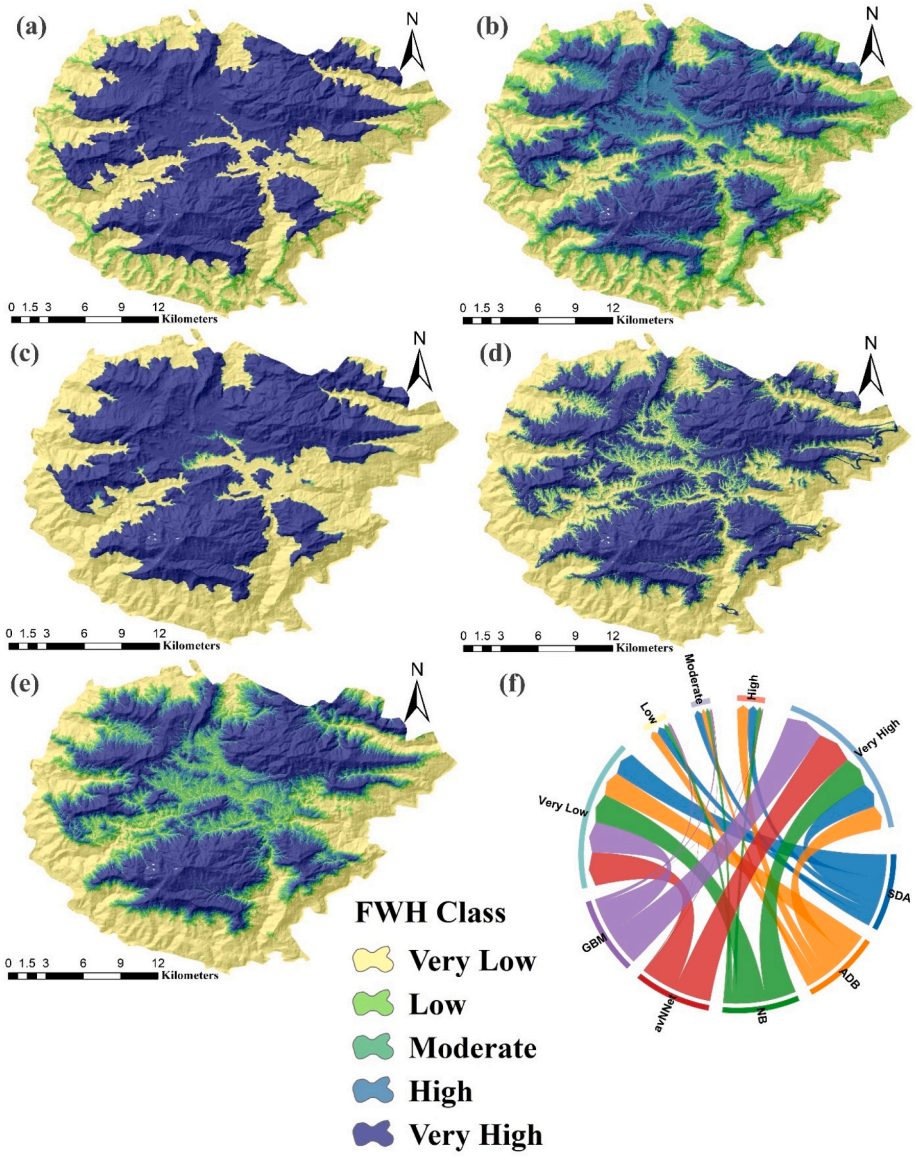

Fig. 12. Future FWH distribution maps and area coverage for SSP5-8.5 scenario (a) GBM model, (b) ADB model, (c) avNNet model, (d) NB model, and (e) SDA model and (f) chord diagram for area coverage.

such as mesh collectors and storage systems, requires substantial investment and poses logistical challenges in remote, rugged terrains. Additionally, maintenance and durability issues may arise in the absence of local technical support. Sociocultural factors are also significant: in communities such as the Van Gujjars and Bhotiya, the acceptance of fog-harvested water may depend on perceptions of quality, alignment with traditional practices, and trust in the technology. Community-engaged pilot projects that integrate traditional ecological knowledge, capacity building, and local co-design are recommended to address these barriers. Policy support through subsidies, targeted awareness campaigns, and adaptive infrastructure investment can further enhance feasibility.

Temporal limitations in fog occurrence data, primarily collected during peak fog seasons, restrict the ability to fully characterize inter-seasonal variability. The lack of continuous monitoring infrastructure, such as visibility sensors or automated fog detectors, may lead to spatial biases. Despite efforts to minimize these through ensemble modeling and metaheuristic feature selection, future research should prioritize the integration of real-time Internet of Things (IoT) sensor networks, multi-season and multi-year observational campaigns, and remote sensing–based fog detection techniques (e.g., MODIS indices; (Werner et al., 2022)). Such advancements would improve the temporal resolution, spatial accuracy, and overall reliability of FWH suitability assessments under changing climate regimes.

The ML-based models used in this study infer relationships between environmental variables and fog occurrence. However, fog formation involves complex physical processes driven by interactions among temperature, humidity, atmospheric stability, wind, topography, and microclimate. Therefore, the suitability maps produced should be regarded as indicative or a rough estimate rather than definitive. Integrating physically informed models with field observations, remote sensing data, and real-time monitoring can improve future studies' assessments of FWH potential.

Ethical approval

This article contains no studies with human participants or animals performed by authors.

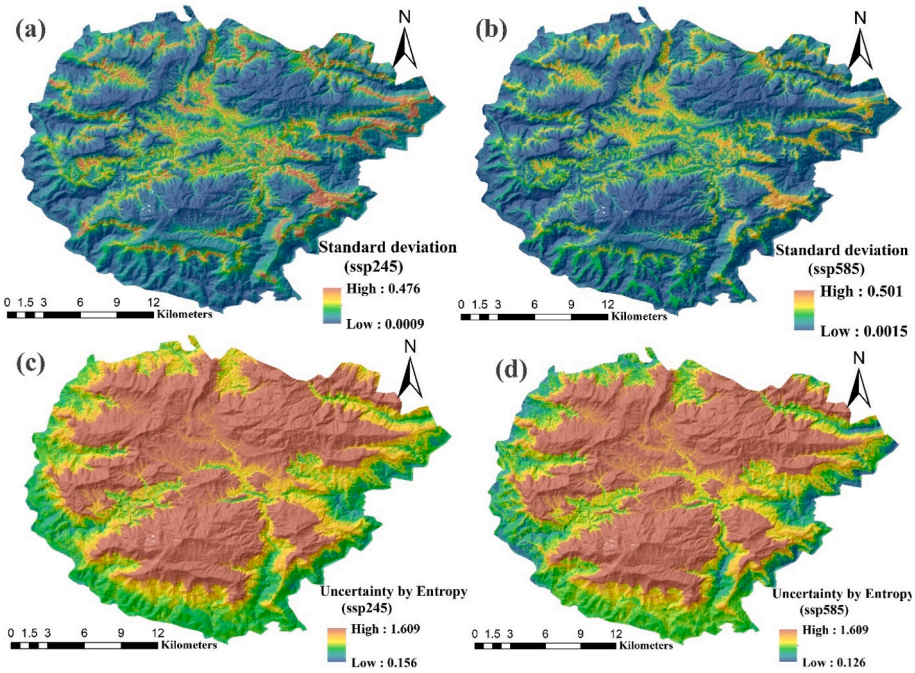

Fig. 13. Projected uncertainty in future FWH maps: (a) Std. Under the SSP2-4.5 scenario, (b) Std. Under the SSP5-8.5 scenario, (c) uncertainty for SSP2-4.5, and (d) uncertainty for SSP5-8.5.

CRediT authorship contribution statement

Chiranjit Singha: Writing – review & editing, Writing – original draft, Visualization, Validation, Software, Methodology, Formal analysis, Data curation, Conceptualization. **Kishore Chandra Swain:** Writing – review & editing, Writing – original draft, Methodology, Formal analysis, Conceptualization. **Biswajeet Pradhan:** Writing – original draft, Validation, Methodology, Investigation, Formal analysis, Conceptualization. **Armin Moghimi:** Writing – review & editing, Writing – original draft, Validation, Formal analysis, Conceptualization. **Babak Ranjgar:** Writing – review & editing, Writing – original draft, Project administration, Investigation. **Shahid Gulzar:** Writing – review & editing, Supervision. **Hetvi Shah:** Writing – review & editing, Formal analysis.

Consent to participate

Not applicable.

Consent to publish

Not applicable.

Informed consent

Not applicable.

Compliance with ethical standards

The authors have no relevant financial or non-financial interests to disclose.

Availability of data and materials

The data supporting this study's findings are available from the author, [Chiranjit Singha, singha.chiranjit@gmail.com], upon reasonable request.

Funding

The authors declare that no funds, grants, or other support were received during the preparation of this manuscript.

Declaration of competing interest

The authors declare that they have no known competing financial interests or personal relationships that could have appeared to influence the work reported in this paper.

Appedix A. Supplementary data

Supplementary data to this article can be found online at https://doi.org/10.1016/j.pce.2025.104138.

Data availability

Data will be made available on request.

References

Aayog, N., 2019. Composite Water Management Index. Ministry of Jal Shakti and India: Ministry of Rural Development. https://social.niti.gov. (Accessed 20 April 2023).

Agam, N., Berliner, P., 2005. Dew formation and water vapor adsorption in semi-arid environments—A review. J. Arid Environ. 65 (4), 572–590. https://doi.org/10.1016/j.jaridenv.2005.09.004.

Agosta, E.A., Corell, D., Estrela, M.J., 2025. Year-to-year fluctuations in fog-water collection in central Mediterranean Iberian Peninsula and the influential large-scale tropospheric circulation patterns. Atmos. Res., 108210 https://doi.org/10.1016/j.atmosres.2025.108210.

Al-Jawad, J.Y., Alsaffar, H.M., Bertram, D., Kalin, R.M., 2019. A comprehensive optimum integrated water resources management approach for multidisciplinary water resources management problems. J. Environ. Manag. 239, 211–224. https://doi.org/10.1016/j.jenvman.2019.03.045. PMID: 30901699.

ASEAN, 2015. ASEAN cooperation on climate change. http://environment.asean.org/asean-working-group-on-climate-change/. Accessed March 2023.

Bai, S., Chao, L., Pan, A., Ho, T., Lin, K., Tso, C., 2024. Study of the relative humidity effects on the water condensation performance of adsorption-based atmospheric water harvesting using passive radiative condensers. Appl. Therm. Eng. 244, 122702. https://doi.org/10.1016/j.applthermaleng.2024.122702.

Baldocchi, D., Waller, E., 2014. Winter fog is decreasing in the fruit growing region of the central valley of California: decreasing FOG. Geophys. Res. Lett. 41 (9), 3251–3256. https://doi.org/10.1002/2014GL060018.
Batisha, A.F., 2015. Feasibility and sustainability of fog harvesting. Sustainability of Water Quality and Ecology 6, 1–10. https://doi.org/10.1016/j.swaqe.2015.01.002.
Böhner, J., Antonić, O., 2009. Land-surface parameters specific to topo-climatology. Dev. Soil Sci. 33, 195–226. https://doi.org/10.1016/S0166-2481(08)00008-1.
Caldas, L., Andaloro, A., Calafiore, G., Munechika, K., Cabrini, S., 2018. Water harvesting from fog using building envelopes: part I. Water Environ. J. 32 (4), 493–499. https://doi.org/10.1111/wej.12335.
Carvajal, D., Mora-Carreño, M., Sandoval, C., Espinoza, S., 2021. Assessing fog water collection in the coastal mountain range of Antofagasta, Chile. J. Arid Environ. 198, 104679. https://doi.org/10.1016/j.jaridenv.2021.104679.
Castelli, G., Cuni Sanchez, A., Mestrallet, A., Montaño, L.C., López de Armentia, T., Salbitano, F., Bresci, E., 2023. Fog as unconventional water resource: mapping fog occurrence and fog collection potential for food security in Southern Bolivia. J. Arid Environ. 208, 104884. https://doi.org/10.1016/j.jaridenv.2022.104884.
Chapman, T.G., 1986. Entropy as a measure of hydrologic data uncertainty and model performance. J. Hydrol. 85, 111–126.
Chauniyal, D.D., Dutta, S., 2018. Application of topographic position index for classification of landforms in Dudhatoli region of Garhwal Himalaya, Uttarakhand. J Indian Geomorphol 6, 28–41.
Cheng, Y., Zhang, S., Liu, S., Huang, J., Zhang, Z., Wang, X., Yu, Z., Li, S., Chen, Z., Zhao, Y., Lai, Y., Qian, X., Xiao, C., 2021. Fog catcher brushes with environmental friendly slippery aluminamicro-needle structured surface for efficient fog-harvesting. J. Clean. Prod. 315, 127862. https://doi.org/10.1016/j.jclepro.2021.127862.
Choudhury, S., Rajpal, H., Saraf, A.K., Panda, S., 2007. Technical Note: mapping and forecasting of north Indian winter fog: an application of spatial technologies. Int. J. Rem. Sens. 28 (16), 3649–3663. https://doi.org/10.1080/01431160600993470.
Cui, T., Li, C., Tian, F., 2021. Evaluation of temperature and precipitation simulations in CMIP6 models over the Tibetan Plateau. Earth Space Sci. 8 (7). https://doi.org/10.1029/2020ea001620.
Domen, J.K., Stringfellow, W.T., Camarillo, M.K., Gulati, S., 2013. Fog water as an alternative and sustainable water resource. Clean Technol. Environ. Policy 16, 235–249. https://doi.org/10.1007/s10098-013-0645-z.
Elashmawy, M., 2020. Experimental study on water extraction from atmospheric air using tubular solar still. J. Clean. Prod. 249, 119322. https://doi.org/10.1016/j.jclepro.2019.119322.
Ermida, S.L., Soares, P., Mantas, V., Göttsche, F.-M., Trigo, I.F., 2020. Google earth engine open-source code for Land surface temperature estimation from the landsat series. Remote Sens. 12 (9), m1471. https://doi.org/10.3390/rs12091471.
Feng, R., Xu, C., Song, F., Wang, F., Wang, X.-L., Wang, Y.-Z., 2020. A bioinspired slippery surface with stable lubricant impregnation for efficient water harvesting. ACS Appl. Mater. Interfaces 12 (10), 12373–12381. https://doi.org/10.1021/acsami.0c00234. PMID: 32048819.
Fessehaye, M., Abdul-Wahab, S.A., Savage, M.J., Kohler, T., Gherezghiher, T., Hurni, H., 2013. Fog-water collection for community use. Renew. Sustain. Energy Rev. 29, 52–62. https://doi.org/10.1016/j.rser.2013.08.063.
Fessehaye, M., Abdul-Wahab, S.A., Savage, M.J., Kohler, T., Tesfay, S., 2015. The potential for scaling up a fog collection system on the eastern escarpment of Eritrea. Mt. Res. Dev. 35 (4), 365–373. https://doi.org/10.1659/MRD-JOURNAL-D-15-00013.1.
Fessehaye, M., Abdul-Wahab, S.A., Savage, M.J., Kohler, T., Gherezghiher, T., Hurni, H., 2017. Assessment of fog-water collection on the eastern escarpment of Eritrea. Water Int. 42 (8), 1022–1036. https://doi.org/10.1080/02508060.2017.1393714.
Friedman, J.H., 2001. Greedy function approximation: a gradient boosting machine. The anna. Stat 29, 1189–1232.
Gandhidasan, P., Abualhamayel, H.I., Patel, F., 2018. Simplified modeling and analysis of the FWHsystem in the Asir region of the Kingdom of Saudi Arabia. Aerosol Air Qual. Res. 18 (1), 200–213. https://doi.org/10.4209/aaqr.2016.11.0481.
Gohil, M., Mehta, D., Shaikh, M., 2024. An integration of geospatial and fuzzy-logic techniques for multi-hazard mapping. Results Eng. 21 (101758). https://doi.org/10.1016/j.rineng.2024.101758.
Guan, X., Burton, H., 2022. Bias-variance tradeoff in machine learning: theoretical formulation and implications to structural engineering applications. Structures 46, 17–30. https://doi.org/10.1016/j.istruc.2022.10.004.
GW, 2023. Ground Water Year Book Uttarakhand, pp. 2021–2022. http://cgwb.gov.in/. (Accessed 20 May 2023).
Haghighi, A.T., Darabi, H., Shahedi, K., Solaimani, K., Kløve, B., 2019. A scenario-based approach for assessing the hydrological impacts of land use and climate change in the marboreh watershed, Iran. Environ. Model. Assess. 1–17.
Han, X., Guo, Z., 2021. Lubricant-infused three-dimensional frame composed of a micro/nanospinous ball cluster structure with salient durability and superior fog harvesting capacity. ACS Appl. Mater. Interfaces 13 (38), 46192–46201. https://doi.org/10.1021/acsami.1c14276. PMID: 34542265.
Henderson, B., Falk, D., 2001. Fog-water collection in Ecuador: an appropriate technology for the rural poor? In: JOHN, S.T. (Ed.), Proceedings of the Second International Conference on FOG and FOG Collection. CANADA, pp. 281–284.
Hoekstra, A.Y., Chapagain, A.K., van Oel, P.R., 2017. Advancing water footprint assessment research: challenges in monitoring progress towards sustainable development Goal 6. Wat 9 (6), 438. https://doi.org/10.3390/w9060438.
Holloway, J., Rudy, A., Lamoureux, S., Treitz, P., 2017. Determining the terrain characteristics related to the surface expression of subsurface water pressurization in permafrost landscapes using susceptibility modeling. Cryosphere 11, 1403–1415. https://doi.org/10.5194/tc-11-1403-2017.
Ismail, Z., Go, Y.I., 2021. Fog-to-water for water scarcity in climate-change hazards hotspots: pilot study in Southeast Asia. Glob Chall 5 (5), 2000036. https://doi.org/10.1002/gch2.202000036. PMID: 33976904.
Jarimi, H., Powell, R., Riffat, S., 2020. Review of sustainable methods for atmospheric water harvesting. Int. J. Low Carbon Technol. 15 (2), 253–276. https://doi.org/10.1093/ijlct/ctz072.
Jenks, G.F., 1967. The data model concept in statistical mapping. Int. Yearb. Cartogr. 7, 186–190.
Jenness, J., 2006. Topographic Position Index (TPI) extension for ArcView 3.x, v. 1.3a. Jenness enterprises. https://www.jennessent.com/arcview/tpi.htm.
Jiao, Z., Ren, H., Mu, X., Zhao, J., Wang, T., Dong, J., 2019. Evaluation of four Sky View factor algorithms using digital surface and elevation model data. Earth Space Sci. 6 (2), 222–237. https://doi.org/10.1029/2018ea000475.
Karimidastenaei, Z., Torabi Haghighi, A., Rahmati, O., Rasouli, K., Rozbeh, S., Pirnia, A., Pradhan, B., Kløve, B., 2019. Fog-water harvesting Capability Index (FCI) mapping for a semi-humid catchment based on socio-environmental variables and using artificial intelligence algorithms. Sci. Total Environ. 708, 135115. https://doi.org/10.1016/j.scitotenv.2019.135115.
Kaseke, K.F., Wang, L., 2018. Fog and dew as potable water resources: maximizing harvesting potential and water quality concerns. GeoHealth 2 (10), 327–332. https://doi.org/10.1029/2018gh000171.
Keim-Vera, K., Lobos-Roco, F., Aguirre, I., Merino, C., del Río, C., 2024. Fog types frequency and their collectable water potential in the Atacama Desert. Atmos. Res. 312, 107747.
Khoury, D., Millet, M., Jabali, Y., Delhomme, O., 2023. Fog water: a general review of its physical and chemical aspects. Environ. Times 10 (12), 224. https://doi.org/10.3390/environments10120224.
Kim, J.H., 2019. Multicollinearity and misleading statistical results. Korean J. Anesthesiol. 72 (6), 558–569. https://doi.org/10.4097/kja.19087.
Kursa, M.B., Rudnicki, W.R., 2010. Feature selection with the Boruta package. J. Stat. Software 36 (11), 1–13. https://doi.org/10.18637/jss.v036.i11.
Kutty, S.G., Agnihotri, G., Dimri, A.P., Gultepe, I., 2014. Fog occurrence and associated meteorological factors over Kempegowda international airport, India. Pure Appl. Geophys. 1–12.
Lange, C.A., Matschullat, J., Zimmermann, F., Sterzik, G., Wienhaus, O., 2003. Fog frequency and chemical composition of fog water—a relevant contribution to atmospheric deposition in the eastern Erzgebirge, Germany. Atmos. Environ. 37 (26), 3731–3739.
LeBoeuf, R., de la Jara, E., 2014. Quantitative goals for large-scale fog collection projects as a sustainable freshwater resource in northern Chile. Water Int. 39 (4), 431–450. https://doi.org/10.1080/02508060.2014.923257.
Lee, J., Lee, W.S., Jung, H., Jung, H., Lee, S.G., 2022. Comparison between total least squares and ordinary least squares in obtaining the linear relationship between stable water isotopes. Geosci Lett 9 (1), 11. https://doi.org/10.1186/s40562-022-00219-w.
Lybarger, N.D., Smith, A., Newman, A.J., Gutmann, E.D., Wood, A.W., Frans, C.D., Warner, M.D., Arnold, J.R., 2024. Improving earth system model selection Methodologies for projecting hydroclimatic change: case study in the Pacific Northwest. J. Geophys. Res. Atmos. 129 (7). https://doi.org/10.1029/2023jd039774.
Marzol, M.V., Sanchez, J., 2008. Fog-water harvesting in Ifni, Morocco. An assessment of potential and demand. Erde 139 (1–2), 97–119.
Mehravar, S., Razavi-Termeh, S.V., Moghimi, A., Ranjgar, B., Foroughnia, F., Amani, M., 2023. Flood susceptibility mapping using multi-temporal SAR imagery and novel integration of nature-inspired algorithms into support vector regression. J. Hydrol. 617, 129100. https://doi.org/10.1016/j.jhydrol.2023.129100.
Mistry, K., Hurst, G.A., 2022. A simple setup to explore fog harvesting as a clean and sustainable source of water. J Chem. Educ. 99 (10), 3553–3557. https://doi.org/10.1021/acs.jchemed.2c00018.
Moghimi, A., Singha, C., Fathi, M., Pirasteh, S., Mohammadzadeh, A., Varshosaz, M., Huang, J., Li, H., 2024. Hybridizing genetic random forest and self-attention based CNN-LSTM algorithms for landslide susceptibility mapping in Darjiling and Kurseong, India. Quaternary Science Advances, 100187. https://doi.org/10.1016/j.qsa.2024.100187.
Nand, M., Sharma, V.C., Maiti, P., 2017. Water crisis in Uttarakhand, ENVIS. Newsl Himalayan Ecol 14 (1).
Natekin, A., Knoll, A., 2013. Gradient boosting machines, a tutorial. Front. Neurorob. 4 (7), 21. https://doi.org/10.3389/fnbot.2013.00021. PMID: 24409142. PMCID: PMC3885826.
Olaf, C., Benjamin, B., Michael, B., Helge, D., Elke, F., Gerlitz, L., et al., 2015. System for Automated Geoscientific Analyses (SAGA) v. Geosci. Model Dev. Discuss. (GMDD) 8, 2271–2312. https://doi.org/10.5194/gmdd-8-2271-2015.
Olcinal, J., 2013. A data driven study of relationships between relief and farmland abandonment in a Mediterranean region. Ecosyst Sustain Dev 9, 175–219.
Olivier, J., 2002. Fog-water harvesting along the West Coast of South Africa: a feasibility study. Water Sci. Appl. 28 (4), 349–360. https://doi.org/10.4314/wsa.v28i4.4908.
Pilié, R.J., Mack, E.J., Kocmond, W.C., Eadie, W.J., Rogers, C.W., 1975. The life cycle of Valley Fog. Part II: fog microphysics. J. Appl. Meteorol. 14, 364–374.
Preetha, P., Bathi, J.R., Kumar, M., Kode, V.R., 2025. Predictive Tools and Advances in Sustainable water Resources through atmospheric water Generation under changing Climate: a review. Sustainability 17 (4), 1462. https://doi.org/10.3390/su17041462.
Pretorius, E., 2009. Using GIS in the search for suitable sites for the implementation of fog water collection systems in South Africa. A Paper Presented at the 24thInternational Cartographic Conference (ICC 2009) in Santiago, Chile.

Pu, Z., Pardyjak, E.R., Hoch, S.W., Gultepe, I., Hallar, A.G., Perelet, A., et al., 2023. Cold fog amongst complex terrain. Bull. Am. Meteorol. Soc. 104 (11), E2030–E2052.
Qadir, M., Jiménez, G.C., Farnum, R.L., Dodson, L.L., Smakhtin, V., 2018. Fog water collection: challenges beyond technology. Water 10 (4), 372–377. https://doi.org/10.3390/w10040372.
Qadir, M., Jiménez, G.C., Farnum, R.L., Trautwein, P., 2021. Research history and functional systems of fog water harvesting. Front Water 3, 145. https://doi.org/10.3389/frwa.2021.675269.
Qiao, N., Zhang, L., Huang, C., Jiao, W., Maggs-Kölling, G., Marais, E., Wang, L., 2020. Satellite observed positive impacts of fog on vegetation. Geophys. Res. Lett. 47 (12). https://doi.org/10.1029/2020gl088428.
Riley, S.J., DeGloria, S.D., Elliot, R., 1999a. Index that quantifies topographic heterogeneity. Intermt. J. Sci. 5 (1–4), 23–27.
Riley, S.J., DeGloria, S.D., Elliot, R., 1999b. A terrain ruggedness index that quantifies topographic heterogeneity. Intermt. J. Sci. 5 (1–4), 23–27.
Ripley, B.D., 1996. Pattern Recognition and Neural Networks. Cambridge publication, p. 184.
Ripley, B.D., 2007. Pattern Recognition and Neural Networks. Cambridge, UK: Cambridge University Press.
Rish, I., 2001. An Empirical Study of the Naive Bayes Classifier in Comput. Scien. Corpus. ID: 14891965.
Ritter, A., Regalado, C.M., Guerra, J.C., 2015. Quantification of fog water collection in three locations of Tenerife (Canary Islands). Wat 7 (7), 3306–3319. https://doi.org/10.3390/w7073306.
Sahoo, S., Singha, C., Govind, A., Moghimi, A., 2025. Review of climate-resilient agriculture for ensuring food security: sustainability opportunities and challenges of India. Environmental and Sustainability Indicators, 100544. https://doi.org/10.1016/j.indic.2024.100544.
Sánchez-Falfan, A., Esperón-Rodríguez, M., Cervantes-Pérez, J., Ballinas, M., Barradas, V. L., 2023. How Important are Fog and the Cloud Forest as a Water Supply in Eastern Mexico? Wat15, p. 1286. https://doi.org/10.3390/w15071286, 7.
Schemenauer, R.S., Cereceda, P., 1994. A proposed standard fog collector for use in high-elevation regions. J. Appl. Meteorol. 33 (11), 1313–1322.
Schneider, K.A., 2025. An entropy model of decision uncertainty. J. Math. Psychol. 125, 102919. https://doi.org/10.1016/j.jmp.2025.102919.
Shanyengana, E.S., Sanderson, R.D., Seely, M.K., Schemenauer, R.S., 2003. Testing greenhouse shade nets in collection of fog for water supply. J. Water Supply Res. Technol. - Aqua 52 (3), 237–241. https://doi.org/10.2166/aqua.2003.0023.
Siabi, E.K., Awafo, E.A., Kabo-Bah, A.T., Derkyi, N.S.A., Akpoti, K., Mortey, E.M., Yazdanie, M., 2023. Assessment of Shared Socioeconomic Pathway (SSP) climate scenarios and its impacts on the Greater Accra region. Urban Clim. 49, 101432. https://doi.org/10.1016/j.uclim.2023.101432.
Singh, V.K., 2016. Water Crisis in Uttarakhand. A Report by Research Foundation for Science, Technol. Ecol. Nat Commun Wom, pp. 27–55.
Singh, P., Dobhal, R., Seth, R., Aswal, R.S., Singh, R., Uniyal, D., Sharma, B., 2015. Spatial and temporal variations in surface water quality of Pithoragarh District, Uttarakhand (India). Anal Chem Lett 5 (5), 267–290. https://doi.org/10.1080/22297928.2016.1140592.
Singh, P., Vaidya, M.K., Guleria, A., Adhale, P., Bhoi, P.B., Bhoi, A.K., Barsocchi, P., 2025. Climatic vulnerability and adaptation strategies for vegetable production in the Northern Himalayan region. Sci. Total Environ. 969, 178343. https://doi.org/10.1016/j.scitotenv.2024.178343.
Singha, C., Sahoo, S., Tinh, N.D., Ditthakit, P., Lu, Q., El-Magd, S.A., Swain, K.C., 2024. Climate-resilient strategies for sustainable groundwater management in Mahanadi River basin of Eastern India. Acta Geophys. https://doi.org/10.1007/s11600-024-01466-5.
Singha, Chiranjit, Sahoo, Satiprasad, Bahrami Mahtaj, Alireza, Moghimi, Armin, Welzel, Mario, Govind, Ajit, 2025. Advancing flood risk assessment: multitemporal SAR-based flood inventory generation using transfer learning and hybrid fuzzy-AHP-machine learning for flood susceptibility mapping in the Mahananda River Basin. J. Environ. Manag. 380, 124972. https://doi.org/10.1016/j.jenvman.2025.124972.
Sun, J., Jia, M.Y., Li, H., 2011. Adaboost ensemble for financial distress prediction: an empirical comparison with data from Chinese listed companies. Expert Syst. Appl. 38 (8), 9305–9312. https://doi.org/10.1016/j.eswa.2011.01.042.
Thrasher, B., Maurer, E.P., McKellar, C., Duffy, P.B., 2012. Technical note: bias correcting climate model simulated daily temperature extremes with quantile mapping. Hydrol Earth Syst Sci [Technical note] 16 (9), 3309–3314. https://doi.org/10.5194/hess-16-3309-2012.
Vanham, D., 2016. Does the water footprint concept provide relevant information to address the water–food–energy –ecosystem nexus? Ecosyst. Serv. 17, 298–307. https://doi.org/10.1016/j.ecoser.2015.08.003.
Verbrugghe, N., Khan, A.Z., 2023. Water harvesting through fog collectors: a review of conceptual, experimental and operational aspects. Int. J. Low Carbon Technol. 18, 392–403. https://doi.org/10.1093/ijlct/ctac129.
Werner, Z., Choi, C.T.H., Winter, A., Vorster, A.G., Berger, A., O'Shea, K., et al., 2022. MODIS sensors can monitor spatiotemporal trends in fog and low cloud cover at 1 km spatial resolution along the US Pacific Coast. Remote Sens. Appl.: Society and Environment 28, 100832. https://doi.org/10.1016/j.rsase.2022.100832.
Williams, A.P., Schwartz, R.E., Iacobellis, S., Seager, R., Cook, B.I., Still, C.J., Husak, G., Michaelsen, J., 2015. Urbanization causes increased cloud base height and decreased fog in coastal Southern California. Geophys. Res. Lett. 42 (5), 1527–1536. https://doi.org/10.1002/2015GL063266.
World Health Organization (WHO), 2023. Drinking water. https://www.who.int/en/news-room/fact-sheets/detail/drinking-water. (Accessed 20 May 2023).
Yu, Z., Li, S., Liu, M., Zhu, R., Yu, M., Dong, X., Sun, Y., Fu, S., 2021. A dual-biomimetic knitted fabric with a manipulable structure and wettability for highly efficient fog harvesting. J. Mater. Chem. A 10 (1), 304–312. https://doi.org/10.1039/D1TA08295G.
Zhou, L., Dai, Y., 2017. How smog awareness influences public acceptance of congestion charge policies. Sustainability 9 (9), 1579. https://doi.org/10.3390/su9091579.
Zuber, V., Strimmer, K., 2009. Gene ranking and biomarker discovery under correlation. Bioinformatics (Edam) 25 (20), 2700–2707. https://doi.org/10.1093/bioinformatics/btp460. PMID: 19648135.